submitted to *Geophys. J. Int.*

Visualizing Best and Worst Case Scenarios in Joint, Constrained, and Time-Dependent Inversions I: Null-Space Transfer and Image-Space Contradictions

Alex Hobé[1]*, Ari Tryggvason[1]

Uppsala University, Department of Earth Science, Uppsala, Sweden

Submitted 30.05.2022

SUMMARY

Because geophysical inversion is used in many vital societal applications, it is unfortunate that some aspects of inverse methods are so abstract. The difficulty of identifying fundamental behaviors is exacerbated when investigating large non-linear problems which combine multiple datasets into a single model, or which produce multiple models with constraints between them. In this first of multiple papers, we investigate and visualize fundamental behaviors of these abstract methods beyond what has been described previously by using simple problems. Instead of using the common resolution description, we use the concepts of the Null Space and Image Space. After providing readers with an intuitive sense of the behaviors of simpler inverse methods, we investigate cases of Joint, Constrained, and Time-Dependent inversion without errors, before moving on to the influence of errors. We then extract the fundamental behaviors of these complex methods from the presented best and worst cases. These new insights allow us to propose four avenues to improve inversion results (including two novel methods), which we present with similar simple problems. Overall, we show the benefits of producing multiple estimated models using constraints over combining the inverse problems into a single model, and, the benefit of visualizing simple problems to uncover deep insights into the fundamentals of our everyday methods.

Key words: Joint inversion – Constrained inversion – Null Space – Time-Dependent Tomography – asynchronous data – Optimized Experimental Design

1 INTRODUCTION

Geophysical inversion is used in many societal applications. These include geothermal energy (e.g., Jousset et al. 2011; Rawlinson et al. 2012; Soyer et al. 2018), groundwater remediation (e.g., Bloem et al. 2020), tunnelling and road building (e.g., Hellman et al. 2017), land-slide risk assessment and mitigation (e.g., Malehmir et al. 2016), permafrost investigations (e.g., Wagner et al. 2019), aquifer characterization (e.g., Doetsch et al. 2010), subduction zone characterization (e.g., Wagner et al. 2007), nuclear site characterization (e.g., Tso 2019), mining exploration (e.g., Astic et al. 2021; Horo et al. 2021), and volcanic (e.g., Paulatto et al. 2019) and tectonic hazard assessment and mitigation (e.g., Hardt & Scherbaum 1994; Kraft et al. 2013; Rawlinson et al. 2012). In these applications, geophysical methods are often used by themselves for individual campaigns, or compared with results from other methods (known as method integration, e.g. Jousset et al. 2011; Malehmir et al. 2016). Improved results can further be obtained using synergies between methods through Joint or Constrained inversion. This can be done using multiple surveys of the same geophysical method (e.g. Julian & Foulger 2010; Horo et al. 2021), and by combining different geophysical methods (Vozoff & Jupp 1975). The latter greatly complicates the interpretation, as the different methods often have different resolutions in time and space, as well as sensitivities to different subsurface properties. Nevertheless, Joint and Constrained inversion have been used to great effect while making the following survey combinations: Seismic Refraction and Electrical Resistance Tomography (ERT; e.g. Doetsch et al. 2010; Hellman et al. 2017; Wagner et al. 2019), ERT and Ground-Penetrating Radar (e.g. Linde et al. 2006), Passive Seismics and Active Seismics (e.g. Wagner et al. 2007), Seismics and Gravimetry (e.g. Paulatto et al. 2019), Receiver Functions and Surface-Wave Dispersion (e.g. Julia et al. 2000), Gravity and Magnetics (e.g. Zhou et al. 2015), Magnetotelluric (MT) and Radio Magnetotelluric (e.g. Commer & Newman 2009),

⋆ Corresponding author: alex.hobe@geo.uu.se

seismic refraction and MT (e.g. Gallardo & Meju 2007), MT and Local Earthquake Tomography (e.g. Demirci et al. 2018). Additionally, frameworks have been and are being developed to combine a larger set of geophysical methods into Joint inversions (e.g. Moorkamp et al. 2011; Rücker et al. 2017), or geologically consistent inversions (e.g. Soyer et al. 2018; de la Varga et al. 2019; Astic et al. 2021).

We highlight Time-Dependent inversion in the title, as this method is applied to the same variable(s) using the same solver, and needs to identify whether differences in the estimated models are significant beyond the known artificial sources of such differences (Hobé et al. 2021). In comparison, the other methods tend to assume an unchanging subsurface and are applied between variables, and/or between methods.

The complex nature of the individual methods and the in-depth knowledge required for using them individually often makes it hard to get a grip on the fundamental processes and influences in Joint and Constrained inversion. Many synthetic investigations have been developed and are used regularly to gain understanding of the accuracy and resolution of these combined methods. These include checkerboard tests, inverting data subsets, and hypothesis tests (inverting a specific synthetic model, see e.g. Koulakov et al. 2013). For time-dependent tomography, feature robustness and the level of artificial differences can be identified using a baseline reconstruction (Hobé et al. 2021), or by using a method for ”ground truthing” (Bloem et al. 2020). Another method for Time-Dependent Tomography we will investigate in detail is inter-model minimization (Julian & Foulger 2010), which we refer to as ”epoch-damping”.

In this paper, we present simple inversion problems to visualize fundamental behaviors in geophysical inversion to ultimately visualize the best and worst case scenarios in Joint, Constrained, and Time-Dependent inversion. The results in this paper are divided into two parts. In Part I, we investigate cases without errors. The Joint, Constrained, and Time-Dependent inversion results are quite complex. Therefore, this part starts with an incremental set of simpler investigations. These investigations both build up towards the complex examples, and help develop the underlying behaviors, which help explain their best and worst cases. In Part II, we investigate the influence of errors. This part relies heavily on the specifics introduced in Part I.

In the discussion, we provide four avenues for improving inversion results, using the fundamental behaviors identified in the results. A non-linear case study investigating these phenomena will be presented in a following paper.

2 METHODS

All the following examples have been produced in Matlab (MATLAB 2021) using Singular Value Decomposition (SVD) and tested using Conjugate Gradients (e.g., Menke 2018). Because of the simplicity of the examples, the results are equivalent within numerical precision.

3 PART I: CASES WITHOUT ERRORS

Before complicating the picture with the inclusion of errors, this Section looks at inversion cases without errors. This Section is divided into two parts. In the first part we establish some vital concepts and vocabulary with a very simple example. We then dive into the best and worst cases for Joint, Constrained, and Time-Dependent inversion for cases without errors in the second part. Experienced readers may skip most of this first part. For a clear understanding of the later Sections, however, we do recommend having a look at the Geometries Section (Section 3.1.2) and the concepts of Null-Space transfer and Image-Space contradictions (Section 3.1.6).

3.1 Build Up Using Simpler Investigations

In this Section, we present simpler investigations, using vital visuals and vocabulary, to prepare for the complex interactions seen in Joint, Constrained, and Time-Dependent inversions. This Section is meant as a visual tutorial to help the reader (especially those unfamiliar with some aspects of geophysical inversion) get an intuitive sense of inversion behavior, which we will rely upon when explaining the more complex cases. We expect experienced readers to also benefit from this visual representation, as we learned a lot ourselves from investigating these methods in this way. First, we introduce the Image Space and Null Space using the simplest possible example in Section 3.1.1. Next, we show the simple geometries and corresponding model-space vectors used throughout most of this paper (Section 3.1.2). We also show how changes in the geometry lead to a reorientation of the model-space vectors. After adding the data-space vectors of one of the geometries, we have all the components required to give an intuitive explanation of how SVD behaves (Section 3.1.3). We then use smoothing to show how constraints change the data-space vectors and how this changes which model-space vectors end up in the result (Section 3.1.4). Here, we describe the fundamental workings of the trade-off curve between roughness and data misfit using the described behaviors. In the last part of this build up (Section 3.1.6), we introduce the concepts of ”Null-Space Transfer” and ”Image-Space Contradictions” using an oversimplified non-linear investigation. Both these concepts help us explain which components of the initial model remain in the final results, as well as describing a downside of using incorrect geometries in non-linear inversion when iterating towards a solution.

3.1.1 The Simplest Example

Fig. 1 shows the simplest possible geometry for a geophysical inversion involving traveltimes. This is an under-determined problem, as there are two unknowns (2 cells) and one data point (1 ray = 1 traveltime). True 1 and True 2 are the two ”model-space vectors” (MSVs) and could represent one possible true model each (except that negative slowness values are nonphysical). Every possible true model for this two-celled example can be reproduced through a linear combination of these orthogonal MSVs. However, only multiples of True 1 can be reproduced using inversion with the geometry at hand. For True 2, the traveltimes of the raypath parts cancel each other out. (Given v21 = 1 km/s, and v22 = -1 km/s, tt2 = dx/v21 + dx/v22 = 0 s.) Therefore, this model component does not affect the data. The set of MSVs that do not affect the data are said to be in the ”Null Space” (NS). In mathematics, the complement of the Null Space is the ”image” (e.g. p. 6 Sharipov 2004), which we will call the Image Space (IS) here (A = IS(A) + NS(A)). Thus, the Image Space (not a commonly used term in geophysics but vital here) is the set of all the MSVs that affect the data.

Consequently, only linear combinations of MSVs in the IS can be reproduced. Therefore, this geometry can only discern the average of the two cells, and never their differences, as there is insufficient data to argue for further model complications (c.f. Occam’s razor). Visually, MSVs in

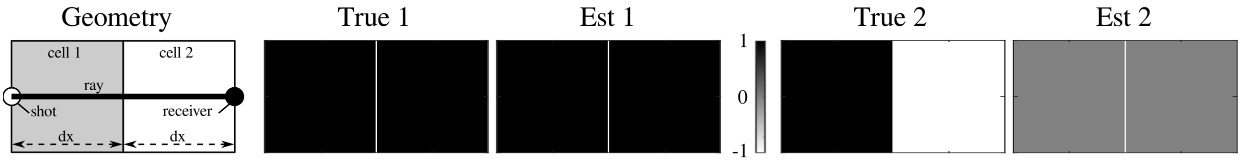

Figure 1. Simplest possible case of an under-determined problem using traveltimes. The two model vectors (True), which combined can produce any possible model using this geometry, and their least-squares inversion using SVD (Est). True 1 lies in the Image Space, and can therefore be reproduced up to numerical precision, whereas True 2 lies in the Null Space. Its estimated model is zero up to numerical precision.

the NS produce model components that are zero up to numerical precision (their corresponding singular values are zero, or near zero). Adding Est 1 and Est 2 is thus basically equivalent to Est 1. Practically, MSVs in the NS are excluded from the inversions using e.g. truncated-SVD, which leads to the same result.

Although our examples in this paper use traveltimes, the same reasoning and insights apply either directly or indirectly to other geophysical methods. To demonstrate this on the simplest level, we may parameterize a gravity experiment using a single measurement and two cells: a top layer above a halfspace. Because there is only one measurement, we would again only be able to produce one density for the entire model. For ERT, we could get a single measurement using e.g. a Schlumberger array. A 2 cell parameterization would again produce the same two MSVs, and we would again only be able to estimate the one uniform resistivity throughout the model.

3.1.2 Geometries

In this paper, we use the geometry in Fig. 2a to show the fundamental behaviors of a range of inversion methods. This geometry (modified from Lévěque et al. 1993) was chosen for it's visual clarity and again presents a seismic traveltime problem. Fig. 2b shows a slight adjustment to the Leveque geometry (compare rec 1 and rec 4). This adjusted geometry is used in the non-linear investigation together with the Leveque geometry to show Null-Space effects arizing in non-linear inversion (Section 3.1.6). We chose the horizontal geometry (Fig. 2c) to provide a maximum difference to the vertical geometry when using Joint, Constrained, and Time-Dependent inversion. All cases assume straight rays between the shots and receivers (dx = dy = 1 km). The orthogonal MSVs (Figure 3) are then produced using SVD of the geometry's G-kernel. Similar to the 2-cell case (Fig. 1) these MSVs can be combined to produce every possible model for this 4x4

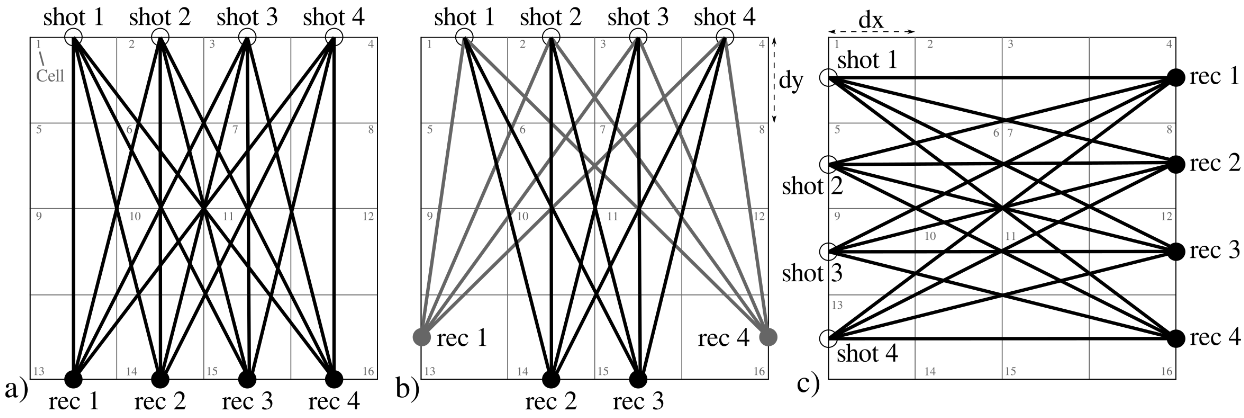

Figure 2. Model geometries. 16 cells with **a)** vertical setup (modified after Lévěque et al. 1993), **b)** adjusted vertical setup, and **c)** horizontal setup.

discretization. These MSVs will be used as our "true" models in this paper. Note that any 4x4 cell parameterization will produce the same set of MSVs reoriented to accommodate the geophysical problem at hand. In other words, the MSVs produced by applying SVD on a 4x4 cell parameterization for any geophysical method, will each be linear combinations of the MSVs in Fig. 3. This is also true of 4x4 nodal parameterizations, though the resulting models would look different due to the interpolation between nodes, the values on the nodes will be linear combinations of the MSVs shown here. **Thus, the main insights in this paper should be reproducible with any other geophysical method (or combination of methods) that employs inversion.**

Table 1 compares the reproducibility of these MSVs between the three geometries. In essence, this table describes what happens if we use a given MSV as the true model to produce synthetic data. For the vertical geometry (Fig. 2a), the first 12 vectors lie in the Image Space (IS), whereas the last four lie in the Null Space (NS). These latter four vectors lie completely in the IS for the horizontal geometry (Fig. 2c). Instead, vectors 4, 5, and 7 lie in the NS of the horizontal geometry. This makes sense, as they are rotated versions of vectors in the vertical geometry's NS (16, 15, and

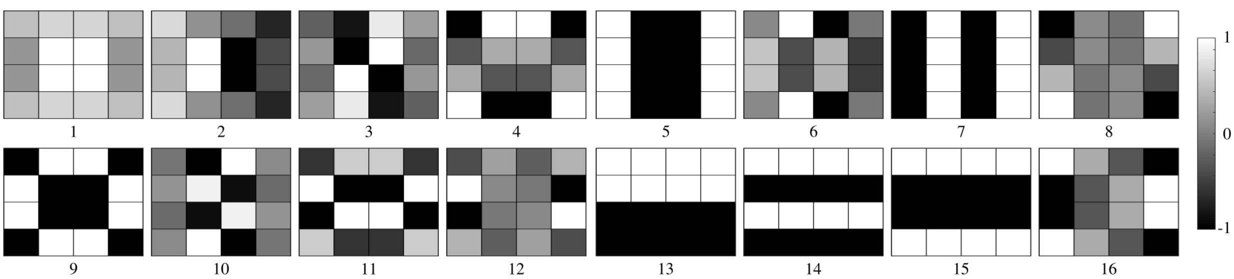

Figure 3. Stretched Model-Space vectors of the vertical geometry (modified from Lévěque et al., 1993).

Table 1. Model-space vector (**MSV**) comparison for the three geometries (**Geom.**) in Fig. 2, using the MSVs of the vertical geometry. MSVs lie in the Image Space (**IS**), Null Space (**NS**), or both (**B**). *98 % NS

Geom. \ MSVs	1	2	3	4	5	6	7	8	9	10	11	12	13	14	15	16
Vertical	IS	IS	IS	IS	IS	IS	IS	IS	IS	IS	IS	IS	NS	NS	NS	NS
Horizontal	B	B	IS	NS	NS	B	NS	IS	IS	IS	B	IS	IS	IS	IS	IS
Vertical adjusted	B	IS	IS	B	B	IS	IS	IS	B	IS	B	IS	B*	B*	B*	IS

14, respectively). In comparison, models 1, 2, 6, and 11 have both IS and NS components using the horizontal geometry. For the adjusted vertical geometry, all vectors lie either in the IS or both in the IS and NS. However, models 13, 14, and 15 lie almost completely in the NS.

The comparisons in Section 3.2 require the orthogonal behavior seen in Table 1 for vectors 4, 5, 7, and 13-16. The SVD algorithm does not produce this ”pure” orthogonality in the MSV. Therefore, slight adjustments were made to these components to remove unwanted contamination and to properly represent vectors 13-16. These vectors were additionally stretched for plotting purposes.

One important take away from Table 1 is the following: A change in the geometry will change which MSVs lie within either the IS or the NS. This is important for Time-dependent inversion, as changes in geometry can thus produce large differences for the same true subsurface. The actual representation of these MSVs after applying SVD on a new geometry can also be linear combinations of the MSVs in the original geometry. Changing between MSV’s for different geometries thus merely represent a re-orientation of the original MSV’s.

Fig. 4 shows the data-space vectors (DSVs) corresponding to the MSVs in Fig. 3 along with the singular values. These orthogonal vectors can be seen as data components of the vertical problem. Using linear combination, these 16 DSVs can produce every possible data vector for the 16 rays. These DSV also each correspond to the data which each MSV would produce. As the DSV themselves are normalized, the singular value is used to scale the DSVs to obtain the synthetic data of each MSV. Vectors 13-16 are clearly in the NS as their singular values are close to numerical precision.

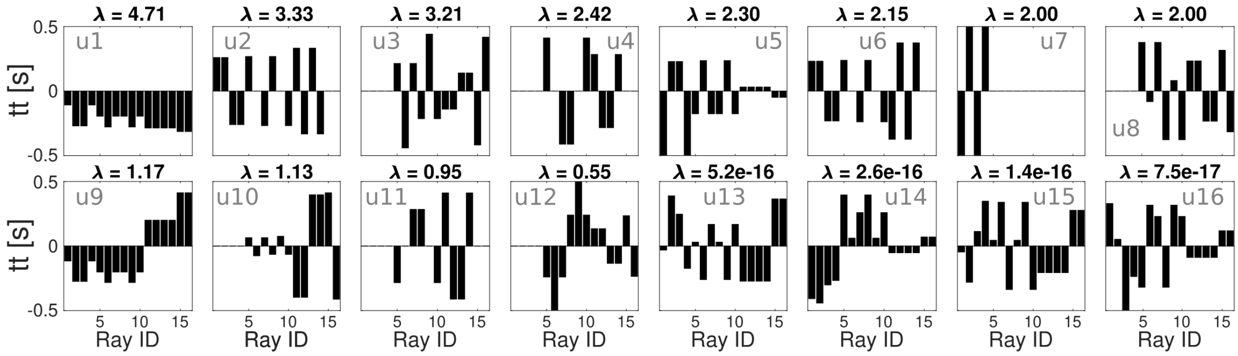

Figure 4. Data-Space vectors corresponding to the Model-Space vectors in Fig. 3. Values at the top of each subplot correspond to that vector's Singular Value.

3.1.3 SVD Behavior

Now that we have all of the required aspects involved in SVD inversion, we will give an intuitive explanation of how SVD translates data into the least-squares estimate.

Eq. 1 shows how the forward kernel, G, (which holds the ray lengths for each cell in our problems) can be decomposed into three matrices, and Eq. 2 shows how to arrange these matrices into the least-squares solution (e.g., Menke 2018):

$$G = USV^T \tag{1}$$

$$m^{Est} = VS^{-1}U^T d^{obs} \tag{2}$$

Here, m^{Est}, is the estimated model, and d^{obs}, the observed data. U, S, and V are explained in Fig. 5. We refer the reader to e.g. Menke (2018) for a mathematical derivation of how SVD decomposes the problem into the individual matrices.

Let us first look at $U^T d^{obs}$ in Eq. 2. Here, a dot product is formed between each DSV and the data. Thus, we check the length of the data in the direction of each DSV. If this length is non-zero, the corresponding MSV will be activated. How much of each MSV is used in the final result is determined by using a weight. This weight is obtained using the singular values as follows: $S^{-1}U^T d^{obs}$. The final estimated model is then obtained by multiplying each MSV with its weight and adding all the resulting model components.

Because a singular value of 1e-16 would produce unrealistically large models, these vectors

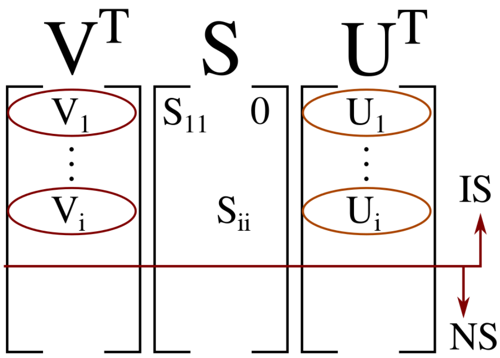

Figure 5. Singular Value Decomposition decomposes the G-kernel into three matrices, V, S, and U. The columns of V hold the model-space vectors, and the columns of U hold the data-space vectors. S is a diagonal matrix which holds the singular values. In this image, the three matrices are oriented to align the Null Space and what we call the Image Space. Note that this orientation does not correspond to either the decomposition of G (Eq. 1), nor the least-squares solution (Eq. 2). The Null Space part of the model space can also be larger or smaller than the Null Space part of the data space.

are usually removed from the equation using truncated-SVD (e.g, Menke 2018). The behavior of SVD can be altered, however, to make use of the Null-Space entries. One way of doing so is to provide constraints, which we will look at next.

3.1.4 Smoothing constraints

Smoothing constraints diminish differences between adjacent cells. These constraints are often used in under-determined (or mixed determined) problems to overcome the ill-posedness of the problem. The problem is thus said to be regularized, which makes the problem behave better during inversion. This also means that we change the question asked of the data. In this Section, we present how such a change in the question fundamentally changes the entries in the U, S, and V matrices. Insights into this allows us to explain how an increase in the smoothing constraints leads to an increase in the data misfit. First we will describe the extension of the kernel and data vector required for smoothing. Implemented as a soft constraint, the smoothing operator multiplied with the model vector equals zero:

$$\begin{bmatrix} G \\ \alpha D \end{bmatrix} m = \begin{pmatrix} d^{obs} \\ \vec{0} \end{pmatrix} \tag{3}$$

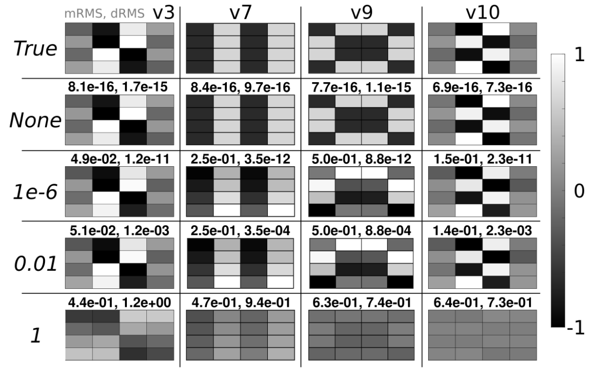

Figure 6. Examples of inversion using the vertical geometry with different levels of smoothing (without, 1e-6, 0.01, and 1) and model-space vectors v3, v7, v9 and v10 as the true models. Values correspond to model misfit RMS (mRMS) and data misfit RMS (dRMS). We note that the model with the highest singular value (v3) is the least affected by the smoothing.

where, D, is the Laplacian operator

$$D_{i,j} = 4m_{i,j} - m_{i-1,j-1} - m_{i-1,j+1} - m_{i+1,j-1} - m_{i+1,j+1} \tag{4}$$

and, α, is the smoothing factor. The Laplacian thus adds one row for every model cell, where index i and j in Eq. 4 are the model cell indices in the x- and y-directions, respectively. Thus, α controls how strongly this regularization is emphasised relative to the data equations. It is important to note here, using the standpoint of image processing, that providing the Laplacian values of the true MSVs (the right side of Eq. 3) would allow us to perfectly reconstruct any model for this geometry. Because these values are not known, we force the solution to be smooth (i.e. the zero entries instead). We visualize the behavior of smoothing regularization with the following synthetic reconstruction tests.

We use the MSVs of the unregularized vertical problem (Fig. 3) as true models, with which we produce synthetic traveltimes. These traveltimes are then inverted using different levels of smoothing (none, 1e-6, 0.01, and 1). Four of the resulting estimated models are shown together with the true models in Fig. 6.

These results show that smoothing constraints come at a cost of both the model misfit (mRMS) and the data misfit (dRMS). The model recovery is poorest for the strongest regularization ($\alpha =$ 1). The recovery at high $alpha$ values diminishes with decreasing singular value (see Fig. 4 for comparison). Fig. 6 also shows that some cell values may increase or decrease, to minimize the

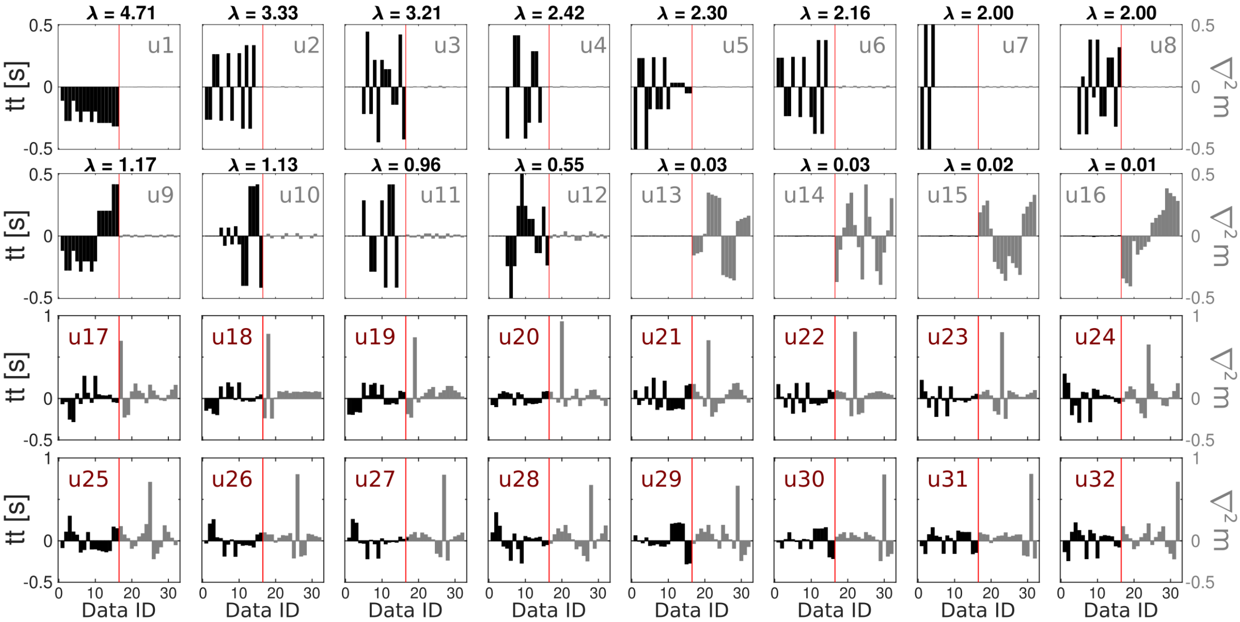

Figure 7. Data-Space vectors (e.g. u1) of the smoothed vertical problem ($\alpha = 0.01$). Values to the left of the red line are normalized traveltimes. Values to the right of the red line are normalized Laplacian values of each cell (i.e. larger values mean larger differences between adjacent cells). These latter values scale with the smoothing factor α. λ values at the top are each vector's singular value. u17-u32 do not have corresponding singular values and thus lie in the Null Space.

impact on dRMS as the estimated models are smoothed out (e.g. $\alpha = 0.01$ for v7 and v9). Next, we will present both the data-space vectors (Fig. 7) and the model weights associated with these synthetic reconstruction tests (Fig. 8), to provide visual clarity of how regularization allows the inversion to contradict the traveltime information.

The added rows in Eq. 3 show up in the data space as additional data-space vectors (Fig. 7): one for each constraint equation in D. Each DSV is also extended beyond the traveltimes (see Fig. 4 for comparison). When looking at the new DSVs (bottom two rows in Fig. 7) there are a few things that stand out. Firstly, the Laplacian entries on the right side of the red line (representing the border between the traveltime data and the Laplacian values) each show a single large spike corresponding to the central cell (see Eq. 4). Secondly, these new DSVs have non-zero values for the traveltime entries. Similarly, non-zero Laplacian values have been added to u1-u16. Their size, relative to the traveltimes, scales with the singular values. Here, DSVs u2, u3, u4, u8 and u11 have ”reversed polarity” relative to the unregularized vertical problem (c.f. Fig. 4). The corresponding MSVs have changed sign accordingly. We also note that u13-u16 no longer reside in the NS ($\lambda \geq 0.01$). In this case, with $\alpha = 0.01$, the singular values are still two orders of magnitude

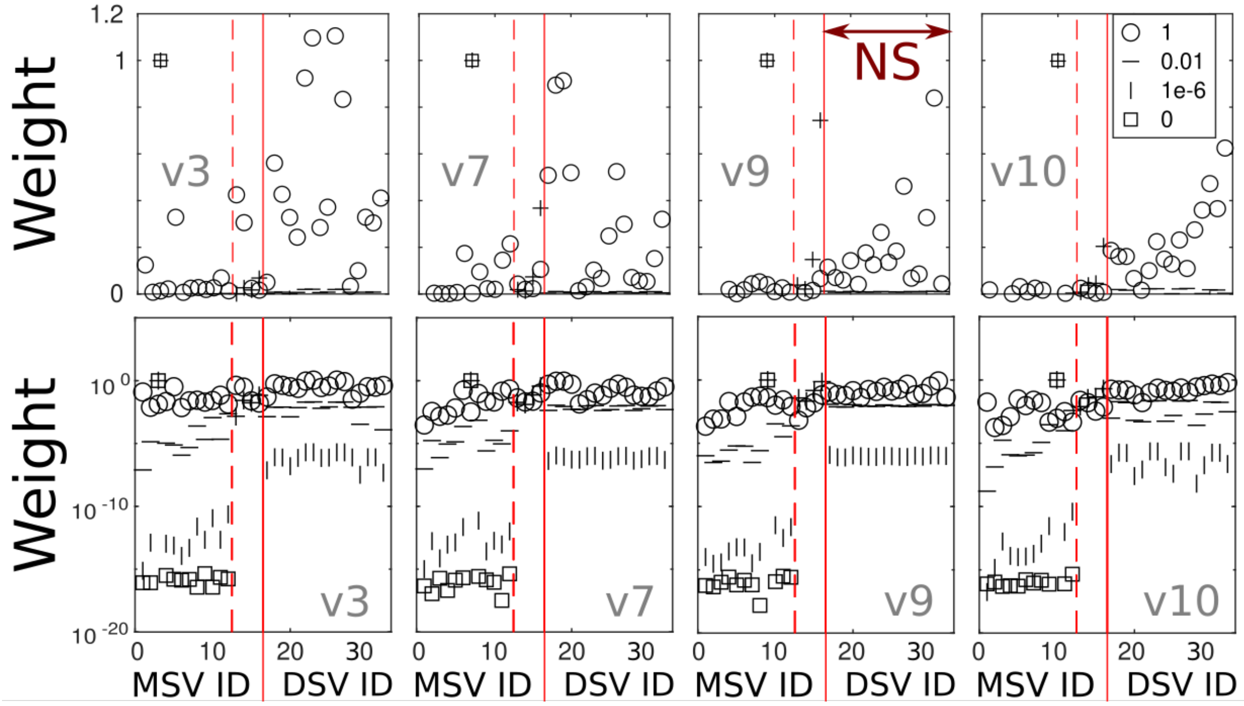

Figure 8. Reconstruction examples at multiple smoothing levels (without, 1e-6, 0.01, and 1) with model components of the vertical problem as true models (e.g. v3). The top and bottom rows are in linear and log-linear scale for emphasis, with the top row not showing values smaller than 1e-3 for visual clarity. To the left of the full red line, these plots show the weights for each of the model-space vectors (MSVs) of the smoothed vertical problem, i.e., how much of each MSV is used when inverting for a given true model. Values between the broken and the full red lines correspond to the four MSVs that are in the NS for the unregularized problem. The values to the right of the full red line instead show how much each DSV in the NS is activated.

smaller than those for u1-u12, but they scale with α. The main contribution of these four DSVs is fitting the Laplacian and less to the travel time data.

The results in Fig. 8 correspond to the four cases in Fig. 6 (see the caption of Fig. 8 for further details). Because Eq. 3 does not change the parameterization (i.e. the size of m), the smoothed vertical problem also has 16 MSVs. As there are 32 DSVs, however, there is more opportunity for the data vector to activate DSVs that do not map onto the estimated model, compared to the unregularized vertical problem.

The results in Figs. 8 show that each reconstruction preferentially activates one MSV when α does not overpower the traveltime contributions (e.g. $\alpha = 1$). (Results for all cases are presented in Appendix A.) When looking at the log-linear view, however, we see that all vectors see increased activation as α increases. Although it is not clear from these images, the weight on the preferentially activated MSV is lowered accordingly (e.g. the weight on MSV 3 for case v3 is lowered by ~1e-5 at $alpha = 1e-6$). Especially interesting is the activation of MSVs between the broken red line and the full red line (see e.g. the apparent pluses in case v9). Even small α values thus activate model components that were in the NS for the unregularized vertical problem.

All of the above observations describe consequences of vector re-orientation. Similar to the vector redistribution when changing the geometry (Table 1), the MSVs of the unregularized vertical problem get redistributed over the new MSVs in the regularized problem. The same occurs for the DSV, except that the traveltime components now get redistributed over 32 DSVs instead of 16. The synthetic data for these reconstructions thus now (partially) activate all DSVs, because each DSV includes a component aligning with the original DSVs. As α increases, more of each original DSV in Fig. 4 is redistributed among all DSVs in the regularized problem (seen as increased activation of all vectors in Fig. 8). As a consequence, all MSVs of the regularized problem are included to some degree in our synthetic reconstructions. As these MSVs also include large parts of the other model components in Fig. 3, their activation incorporates components not included in the true model. The regularized problem thus allows the inclusion of other model components and contradiction to the traveltimes by re-orientating the vectors and having data components map onto the NS of the data.

3.1.5 A closer look at the L-curve

Using these insights and observations we can now explain the behaviors observed in the ”L-curve” commonly used to find a suitable value for α. By plotting dRMS as a function of model roughness (i.e. inverse of smoothness) this trade-off curve behaves as follows. As α increases, the roughness decreases rapidly with a small increase in dRMS (the horizontal part of the L). This behavior switches entirely in the corner of the L, to instead have large increases in dRMS for small further decreases in roughness (the vertical part of the L). As seen in Fig. 7, the MSVs formally in the NS (e.g. MSV 16 for v9) get activated strongly at small α values and to a lesser degree when $\alpha = 1$. When we examine the corresponding vectors u13-u16, we note that the relative amplitude of the constraint values is much larger than the traveltime values, while the opposite occurs for u1-u12. Thus large changes to the estimated models are obtained without incurring penalties in the dRMS by incorporating those MSVs that only affect the data marginally. As α increases, more of the true model vector (e.g. v3) is included in all MSVs, leading to more inclusion of model components that contradict the data. The combined behavior in the two previous sentences explains the horizontal part of the L-curve.

As α increases further, however, all model components get redistributed further, including those that do not affect the data. (All MSVs in the smoothed problem thus map onto both the IS and NS of the unregularized problem.) Activating MSVs 13-16 in the smoothed problem thus incorporates more and more model components that affect the data. The corner of the L signifies the moment where the desired model vector is diluted so much over the available MSVs that several DSVs in the IS are activated significantly at the same time by the desired traveltimes, thus incorporating larger and larger components not included in the true model. This is best seen for v3 (Fig. 8) for $\alpha = 1$. Again, the misfit itself arises from traveltime components activating the NS.

Although this investigation does not directly address the main goal of identifying the best and worst case scenarios of Joint, Constrained, and Time-Dependent inversion, the mechanisms at play are the same. How the IS and NS affect geophysical results is further discussed in the next Sub-Section and will prove to be vital for our main goal.

3.1.6 Non-Linear and Initial Model Investigation

To show the influence of changes in the Image-Space and Null-Space in non-linear inversion, we perform a simplified non-linear investigation. This investigation uses the following steps: 1) Produce synthetic data for one of the model-space vectors in Fig. 3 using the vertical geometry (Fig. 2a), which we will call the final geometry here. 2) Choose an initial model. 3) Produce a model update using the adjusted vertical geometry (Fig. 2b), which we will call the intermediate geometry here. 4) Produce a final model update using the final geometry. This procedure simulates the situation in which we do not know the exact ray path locations.

Five such simulations are shown in Fig. 9. Sims. 1 to 4 use MSV 1 as the true model, and simulation 5 uses MSV 2. Both of these lie in the IS of the vertical geometry. Simultaneously, MSV 2 lies in the IS of the intermediate geometry, whereas MSV 1 lies partly in its NS. The first simulation use a starting model of zero, which essentially means there is no starting model, and is done to show a result free of its influence. Simulation 2 uses a starting model in the IS of the intermediate geometry, which lies in both the IS and NS for the final geometry. Simulation 3 uses a starting model that lies in the IS of the final geometry, and in both the IS and NS of the intermediate geometry. Simulation 4 uses a starting model in the NS of the final geometry, and in both the IS and NS of the intermediate geometry. Simulation 5 uses the same starting model as Simulation 4, and a different true model (see above). Before discussing the results, we explain the contents of each column in Fig. 9.

Each row starts with the chosen initial model and the true model (columns 1 and 2). The next three columns (3-5) break down the intermediate result produced using the intermediate geometry. The first column of the intermediate results (column 3) shows the intermediate model. This model can be decomposed into three components: the true model (column 2), the remainder of the initial model (column 4), and a third component produced by using the wrong geometry (column 5).

The last three columns (6-8) break down the final results using the final geometry in a similar fashion. The first column of the final results (column 6) shows the final models. The next column (7) shows the model component of the initial model which remains in the final result. The last column (8) shows what remains of the component introduced due to the intermediate geometry in the final result.

Simulations 1 and 2 in Fig. 9 have identical intermediate and final models even though their initial models are different. In Simulation 2, the intermediate result is not affected by an initial model, which lies in the IS of that geometry. Because it lies in the IS, the initial model produces synthetic data which contradicts the observations. We call this Image-Space Contradictions. This causes the inversion to resist incorporating this component into the result. From this we conclude that model components of the previous iteration will always be overwritten, if 1) they lie in the current geometry's IS, and 2) the inversion allows it (e.g. smoothing and model-step limitations).

The first two simulations also show that the incorrect geometry introduces a model component in the intermediate result, which is mostly removed by the final geometry. The data misfit of the final result (numerical precision) shows that the remaining component lies in the NS of the final geometry. From this we further conclude that any model component of the previous iteration,

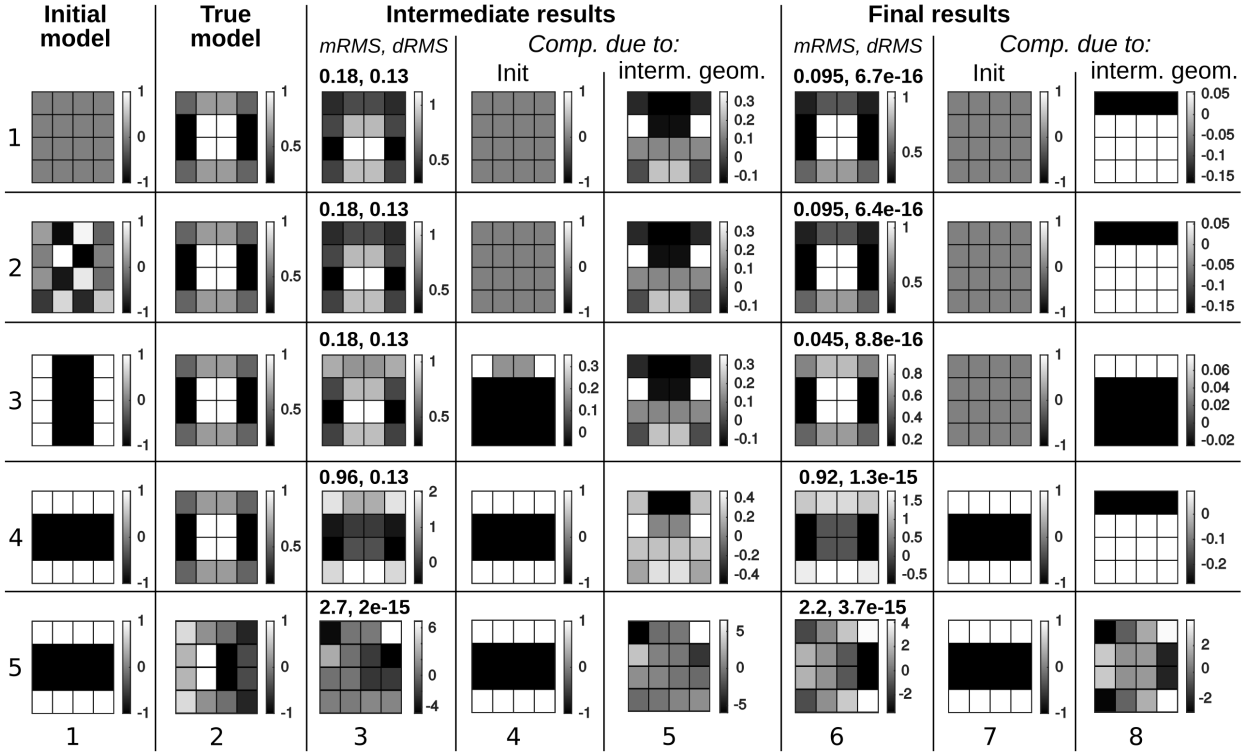

Figure 9. Results of the non-linear investigation using four different starting points. From top to bottom, these are: row 1) zeros everywhere, row 2) a model in the Image Space (IS) of both geometries, row 3) a model in the IS of the vertical geometry and partially in the Null Space (NS) for the intermediate geometry, and row 4 & 5) a model in the NS for the vertical geometry and mostly in the NS for the intermediate geometry. This last case is repeated with a different true model. Shown from left to right: column 1) initial model, col. 2) true model, col. 3) intermediate result using the intermediate geometry, col. 4) remainder of the initial model in the intermediate result, col. 5) remaining component of the intermediate result due to using the intermediate geometry, col. 6) final result using the vertical geometry, col. 7) remainder of the initial model in the final result, and col 8) the remainder of the component due to the intermediate geometry. mRMS and dRMS describe the root-mean-squared misfit of the model and data, respectively. The row numbers correspond to the individual simulations.

that lies in the NS of the current geometry, will always remain. We call this Null-Space Transfer. Note that this true model can be reproduced up to numerical precision when only using the final geometry. The component due to the intermediate geometry is therefore an undesired result of needing to find the correct geometry using non-linear iterations.

In simulation 3, the NS component of the starting model remains in the intermediate result. The final model, however, is unaffected by the initial model. Because the initial model lies completely in the IS of the final geometry, the remaining component in the intermediate model was removed from the final model.

Simulation 4 shows that its initial model affects both the intermediate and the final results. This initial model additionally produces a component in the intermediate geometry which lies in the NS of the final geometry. This component is much larger compared to the component in the other rows. Simulation 5 shows even stronger effects, despite the fact that the true model is in the IS of both geometries. The difference here is that the intermediate geometry would produce different data for this IS component, compared to the true geometry. The dRMS of the intermediate model shows, however, that the synthetic data fully maps onto the IS for the intermediate geometry. This causes a larger component to be activated, a large part of which unfortunately lies in the NS of the final geometry.

Comparing the different simulations, we see from Simulations 1 to 3 that if the starting model has no component in the NS of the final (and true) geometry, there will be no direct effects of the starting model remaining in the final model. The initial model would thus optimally consist of model components which lie in the IS of the final geometry. Whether this is feasible depends on the geophysical method and the geometry. From Simulations 4 and 5 we see that any components of the starting models that lie in the NS of the final geometry will remain in the final model. An additional complication is how the non-linear inversion develops towards a final model. This development is affected by the initial model and could introduce intermediate components which remain in the final NS. We thus conclude that any component in the initial or intermediate models of a non-linear inversion, which consistently lies in the NS of the subsequent geometries, will remain in the final model. We call this unwanted form of Null-Space Transfer: Null-Space Contamination. We also note in Simulations 1 to 4 that the data fit is perfect (within numerical precision), despite the models being rather different. Without knowing the answer before hand, it is of course difficult to judge which model is ”the best”.

The difference between NS Transfer and NS shuttles (e.g., Deal & Nolet 1996; Rowbotham & Pratt 1997) is that NS shuttles are used to get a desired outcome by projecting model features onto the NS and adding them to a given model. This allows practitioners to e.g. add prior knowledge with minimum impact on the data misfit (e.g., Rowbotham & Pratt 1997), quantify uncertainty around the model (e.g., De Wit et al. 2012), and explore the set of acceptable results (e.g., Fichtner & Zunino 2019; Fichtner et al. 2021). NS Transfer, in contrast, is an inherent part of both non-linear inversion, and, as we will see, of Joint, Constrained, and Time-Dependent inversion. The production of new NS components in the intermediate steps is - to our knowledge - missing from descriptions of non-linear inversion in the literature. The closest description of this phenomenon in literature is the propagation of errors in the following equation (modified from Rawlinson & Spakman 2016):

$$\hat{m} = G^{-g}Gm^{true} - G^{-g}Em^{true} + G^{-g}\epsilon \tag{5}$$

With, $\hat{m}$, and m^{true}, the estimated and true models, G and G^{-g} the (linear) G-kernel and its generalized inverse, E, a matrix representing the accumulated errors in the G-kernel due to linearization, and ϵ, an error term combining errors due to linearization, noise, picking, and parameterization. The three terms in Eq. 5 can be reduced to the following conceptual description. $G^{-g}Gm^{true}$ corresponds to the mapping of the true model onto the estimated model. $-G^{-g}Em^{true}$ then subtracts the mapping of the linearization errors in the G-kernel compared to the "true" G-kernel of the true model onto the estimated model. Lastly, $G^{-g}\epsilon$ adds the mapping of all the sources of errors onto the estimated model.

Instead of using the concepts of the IS and NS, Rawlinson & Spakman (2016) use the concept of resolution to describe this error propagation. Whereas the resolution description tends to work as a black box which morphs the data and initial model into the estimated model, the concepts of NS transfer and IS contradictions allow us to clearly describe the fundamental behaviors at each point of the non-linear process based on the IS and NS components of each geometry.

A different issue with non-linear inversion is presented in Simulation 5 in Fig. 9. The intermediate geometry reproduces the data up to numerical precision. As this is the wrong geometry, it produces a very poor intermediate model. Additionally, the NS component remaining in the final geometry is very large for this case. Because of the low data misfit in the intermediate case, it is unclear if the final geometry would even be reached, though the model change would produce a change in geometry and thus in the misfit. Additionally, because this setup is oversimplified, it is unclear if this issue will arise in true non-linear problems. This issue is commonly dealt with in software like, e.g. PStomo_eq (e.g., Tryggvason & Linde 2006), by limiting the maximum size of the model update in a single iteration.

3.2 Joint, Constrained, and Time-Dependent Inversion

Now that we have introduced all the vital concepts, we will move on to visualizing the best and worst case scenarios of Joint, Constrained, and Time-Dependent inversion for cases without errors. First we describe the investigation with which these cases were found. Then we show and discuss cases where Null-Space Transfer dominates. Next we show and discuss cases where IS Contradictions dominate. Lastly, we show and discuss cases where both occur simultaneously. For those readers who skipped ahead, NS Transfer and IS Contradictions are explained in Section 3.1.6.

We will use the following nomenclature to simplify our upcoming discussions. Combined inversion: The group of inversion methods that combine two (or more) datasets, belonging to one (or more) geophysical methods, into one (or more) estimated models. Within combined inversion, there are two categories: those that produce a single model, and those that produce multiple models. We could call these single-model producing methods, and multi-model producing methods. Examples of single-model producing methods include: joint inversion of two ERT arrays (e.g. Horo et al. 2021), and joint inversion of asynchronous data in e.g. local earthquake tomography (e.g. Hobé et al. 2021). Because single-model producing methods is a mouth full, we will use ”joint inversion” throughout this text instead (we join two problems to produce a single model). We fully realize that this is only a subset of the methods that are commonly (and inconsistently) described as ”joint inversion”. Examples of multi-model producing methods include: cross-gradient constraints (e.g. Gallardo & Meju 2004; Gallardo 2007; Tryggvason & Linde 2006; Manukyan et al. 2018), combined inversion using petrophysical relationships (e.g. Haber & Holtzman-Gazit 2013; Wagner et al. 2019), and inter-model minimization (e.g. Julian & Foulger 2010).

3.2.1 Methods and Setup

We use the vertical and horizontal geometries (Fig. 2a and c) to investigate fundamental behaviors of combined inversion methods. The true models for this investigation are all permutations of the MSVs in Fig. 3 (one for each geometry). Using these true models, we first produce synthetic data. This data is then inverted for using Singular Value Decomposition and Conjugate Gradients in conjunction with the following three methods at different levels of regularization: 1) Joint inversion, 2) Inter-model minimization (epoch damping), and 3) Equivalent-gradient constraints. Additionally, the data is inverted for without any regularization, which we call ”single inversion”.

The following two equations describe the implementation of these inversion schemes:

$$\begin{bmatrix} G_1 \\ \alpha G_2 \end{bmatrix} m = \begin{pmatrix} d_1^{obs} \\ \alpha d_2^{obs} \end{pmatrix} \tag{6}$$

$$\begin{bmatrix} G_1 & \vec{0} \\ \vec{0} & G_2 \\ \multicolumn{2}{c}{\alpha D} \end{bmatrix} m = \begin{pmatrix} d_1^{obs} \\ d_2^{obs} \\ \vec{0} \end{pmatrix} \tag{7}$$

Here, G_1 corresponds to the kernel of the vertical geometry, G_2, is the kernel of the horizontal geometry, D is the matrix holding the regularization entries described below, and α is the regularization factor (weight). The regularization factors for each of these combined inversion schemes are: 1, 0.01, 1e-6.

The joint-inversion scheme vertically combines the equations of both geometries and adds a regularization factor to the horizontal geometry equations (G_2 in Eq. 6). Inter-model minimization can be used in Time-Dependent Tomography (Julian & Foulger 2010) and minimizes model differences (i.e. $\alpha * [m1_{ij} - m2_{ij}] = 0$; Eq. 7). Equivalent-gradient constraints (EG) minimizes the differences in absolute model gradients ($\alpha * [\nabla m1_{ij} - \nabla m2_{ij}] = 0$; Eq. 7).

EG is similar to cross-gradient constraints (CG), which minimizes the cross-gradient of the models (e.g. Gallardo & Meju 2004). We show the results for equivalent gradients here, as this is a linear operation and CG is fundamentally non-linear. When comparing EG and CG, CG allows models to have, e.g., negative gradients, or zero gradients, where the other model has a positive gradient. Thus, the behaviors of CG would go beyond the ones described here for EG, while simultaniously being complicated by CG’s non-linearity.

As we have seen in Table 1, MSVs of a given geometry can be completely in the IS, completely in the NS or both. We have run permutations of all MSVs of the vertical geometry (Fig. 2) applied to the two geometries. The next two Sub-Sections show a summary of these hundreds of results into four different categories: 1) Those where both datasets push for the same model. We call this

IS Corroboration. 2) Those where NS transfer occurs. 3) Those where IS Contradictions hinder incorporation of MSVs. And 4) those where a mixture of the other three occurs simultaneously.

3.2.2 MSV Inheritance Without Resistance

Fig. 10 shows cases where MSVs are adopted without resistance, as they do not incur an increase in the data misfit. Table 2 describes these results in detail (Cases 1 to 4). The best case scenarios here all have the same true model for both geometries (Cases 1-3). MSV adoption without resistance can come in two forms. The first has the two geometries corroborate the same result (IS Corroboration; see case 1), i.e. the data for both geometries activate the same IS model component. The other form occurs when Null-Space transfer fills in missing pieces (Cases 2 and 3). In the worst case (4), mutual Null-Space Contamination causes the MSVs to combine into an incorrect model, without providing any signal in the data misfit. Note that all these forms of adoption occur already at the lowest level of regularisation, because there is nothing in the respective data that will resist it.

3.2.3 Resisting Incorporation of MSVs

Fig. 11 shows relevant cases (Case 5 to 7) where MSVs are resisted when they incur an increase in the data misfit. Table 2 describes these results in detail. The incorporation of MSVs that produce IS Contradictions is resisted in every form of coupling shown here. As regularization increases, the contradicting MSVs are forced into the results. In consequence, the result tries to find a new optimum which minimizes the data effects of this adoption. Because of this, the results start to move away from both true models at high levels of regularisation. The Joint inversion of case 7 is especially interesting. Already at low regularization, the horizontal geometry is able to force a model component through the NS into the final result. This is surprising, as the true model lies completely in the IS of the vertical geometry. This shows, that resisting vectors due to IS Contradictions may lead certain components to morph into the closest NS component. That this is not always the case can be seen in Case 5. The behavior of the Joint inversion of Case 7 then continues quite similar to epoch damping and equivalent gradients. As regularization increases, the NS

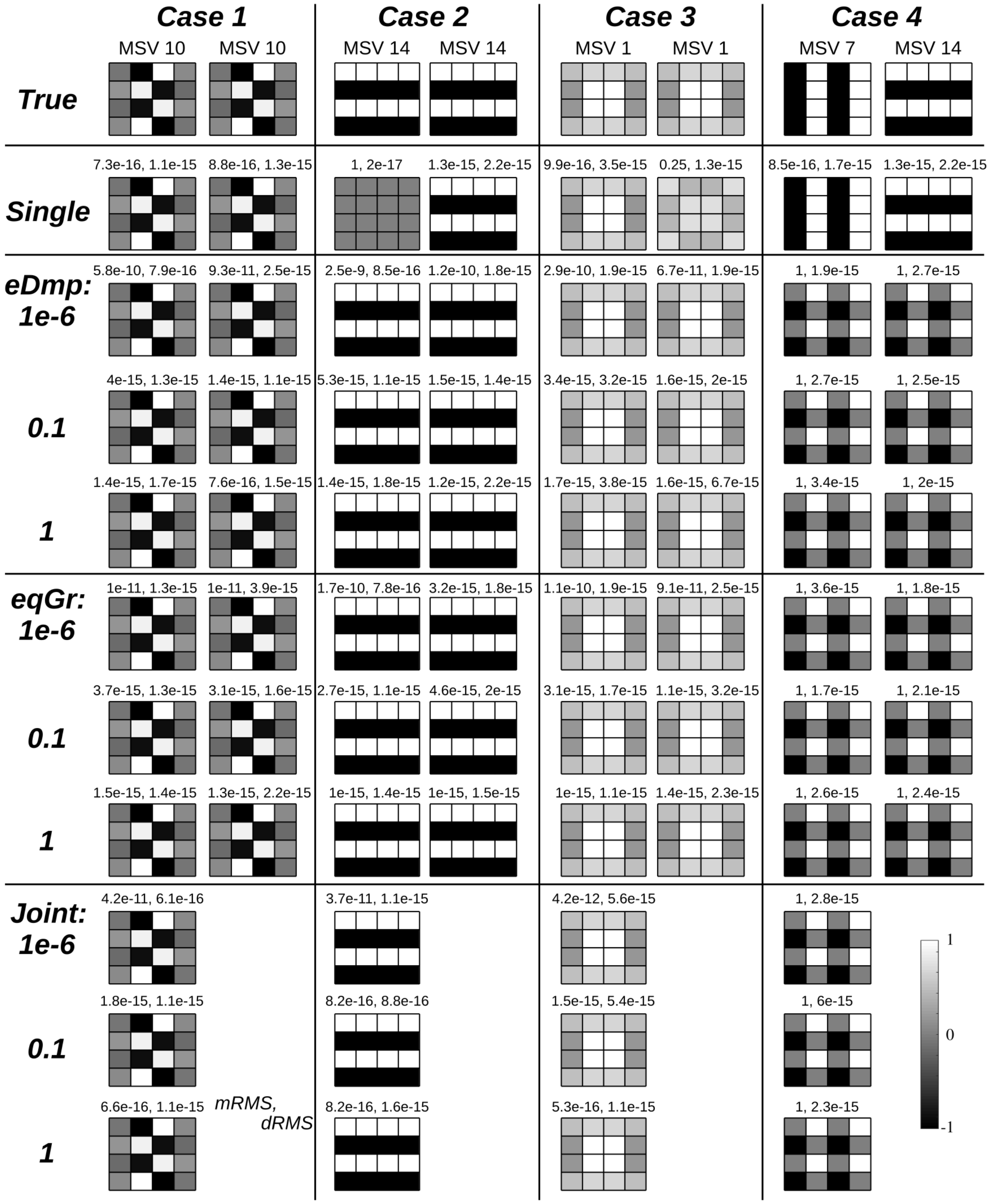

Figure 10. Combined inversion cases 1-4 compared using single inversion, epoch damping, equivalent gradient constraints, and joint inversion. True model numbers correspond to Fig. 3. The two numbers above the estimated models correspond to the model and data RMS misfit (mRMS and dRMS), respectively. All estimated models for case 4 have values up to +/-2, except for the single inversions.

Table 2. Descriptions of the combined inversion behaviors observed in Figs. 10 and 11. **Geom**: Geometry, **MSV**: true Model-Space Vector, **VG**: in which of the Image Space (IS), Null Space (NS), or both (B) the true MSV lies for the vertical geometry, **HG**: in which of the IS, NS, or both the true MSV lies for the horizontal geometry

Case	Geom.	MSV	VG	HG	Behavior
1	V. uses	10	IS	IS	Both geometries corroborate the same result. Neither affect the data misfit.
	H. uses	10	IS	IS	
2	V. uses	14	NS	IS	The missing component for the first geometry is added without resistance. The 2nd geometry thereby completes the image.
	H. uses	14	NS	IS	
3	V. uses	1	IS	B	Similar to case 2 with part of the model being reproduced by the horizontal geometry already.
	H. uses	1	IS	B	
4	V. uses	7	IS	NS	Mutual null-space contamination. Both model vectors are summed together without impacting either data misfits.
	H. uses	14	NS	IS	
5	V. uses	14	NS	IS	The vertical geometry's inversion resists the inclusion of the IS model vector, as it contradicts its data. Increased regularization forces a mutual model, which does not correspond to either true model. The data misfit is strongly affected.
	H. uses	10	IS	IS	
6	V. uses	3	IS	IS	The inversions of both geometries resist the introduction of IS vectors which contradict their data. As in case 5, increased regularization leads to models which correspond to neither true models, and leads to increased data misfit.
	H. uses	10	IS	IS	
7	V. uses	14	NS	IS	The vertical geometry's inversion resists the inclusion of the IS model vector, as it contradicts its data. The combined inversion with the vertical geometry worsens the already poor results of the horizontal geometry.
	H. uses	1	IS	B	
8	V. uses	1	IS	B	The NS component of MSV 1 is adopted in the horizontal model without resistance (nor a signal in the data misfit). Resistance of contradictory IS components again leads to poorer results as regularization increases.
	H. uses	10	IS	IS	

component remains and other components are added due to the IS Contradictions. In Case 6 both geometries resist the IS components of the other geometry, requiring a high level of regularization before the models start deteriorating and resemble the Joint inversion model.

3.2.4 Combinations of Image-Space Contradictions, Corroboration, and Null-Space Transfer

As any true model can be obtained through linear combinations of MSVs, each of the three described behaviors can (and will for large problems) occur simultaneously. As an example, Case 8 combines both NS transfer and IS contradictions. As seen with the other cases, the NS transfer occurs with very little regularization (see e.g. the mRMS for eDmp with $\alpha = 1e - 6$), whereas the IS contradictions cause the result to deform away from both true models with increased regularization. Here again, the Joint inversion case struggles to deal with the contradictions in both datasets. For $\alpha = 1e - 6$, the result again adds the same NS component as in Case 7. This time it is combined with MSV 1. As regularization increases, MSV 10 and MSV 12 are major components here, with other components also coming in.

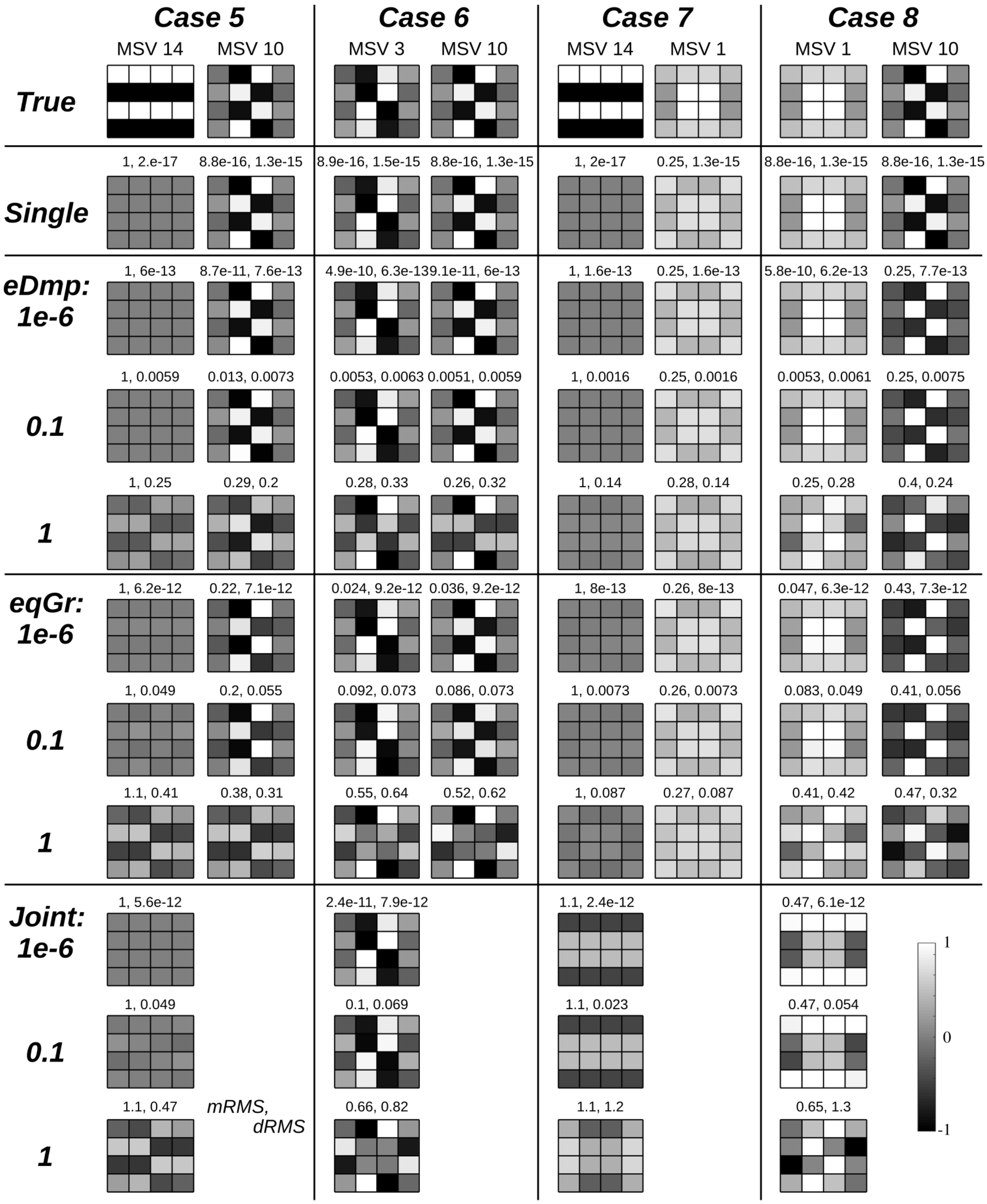

Figure 11. Combined inversion cases 5-8 compared using single inversion, epoch damping, equivalent gradient constraints, and joint inversion. True model numbers correspond to Fig. 3. The two numbers above the estimated models correspond to the model and data RMS misfit, respectively.

Geophysical inversions are generally not solved using a single MSV. Therefore, real investigations using Joint, Constrained, and Time-Dependent inversion would always include some amount of Null-Space Transfer, Image Space Corroboration and Image Space Contradictions. In this section we have seen that NS Transfer occurs at real low levels of coupling between the two models. At the same time, IS Contradictions are harder to impose on the models, as they contradict the data. With the understanding gained in this Section, we may be able to identify each of these three cases by changing the regularization, and by comparing the results with those from single inversions. It is thus fundamental to perform individual inversions for comparison. Additionally, our results point out benefits of producing multiple models using constraints over jointly inverting for one, as well as additionally issues only encountered when jointly inverting for one model. We therefore suggest it is preferred to produce multiple models using a combined inversion method of choice (e.g. epoch damping, cross-gradient constraints, etc.), compared to Joint inversion. If practitioners choose to produce a single model using Joint inversion, however, we suggest it is vital to at least produce multiple models in a combined inversion of choice to check for the robustness of this jointly inverted single model. When looking at real problems, however, these issues are further complicated by data errors, which we will investigate next.

4 PART II: THE INFLUENCE OF DATA ERRORS

It is often repeated, that the influence of data errors scales with the inverse of the singular value. We put this into context by inverting random Gaussian errors and individual outliers. Based on the results, we describe how data errors influence Joint, Constrained, and Time-Dependent inversions.

4.1 Repeated Investigation Using Gaussian Errors

In this investigation, we used the vertical geometry (Fig. 2) to invert for random Gaussian errors 10 000 times (μ = 0 and σ = 1), without including any true data.

$$Gm = \vec{\sigma_e} \tag{8}$$

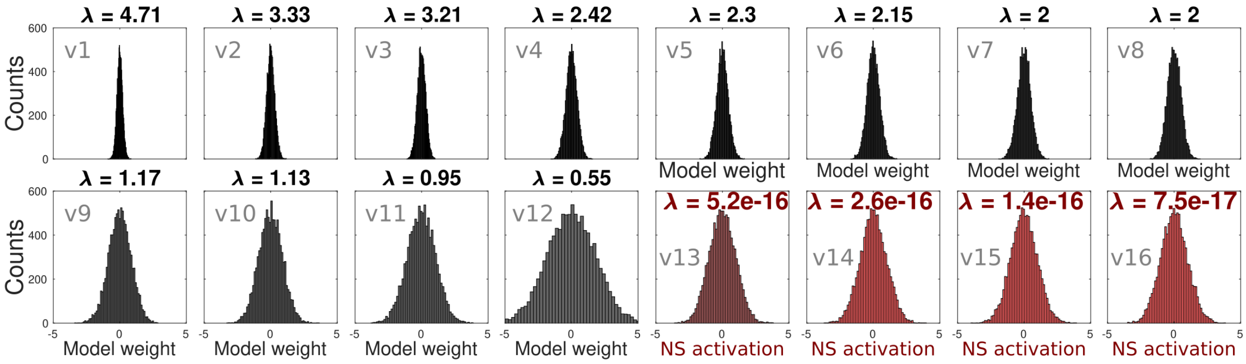

Figure 12. Histograms of model weights for 10 000 iterations of random Gaussian errors. Each count corresponds to a single inversion. Each subplot corresponds to a model-space vector in Fig. 3, except for the last entries in red. Those depict the activation of the data-space vectors instead, as these vectors lie in the Null Space. λ denotes the associated singular value.

with, $\vec{\sigma_e}$, the random errors for each entry. Fig. 12 shows the corresponding model weights for each MSV.

Thus, repeated Gaussian errors produce a bell-curve distribution of these model weights with a mean around zero. As the singular value decreases, the width of the distribution (and thus the possible error) increases. In other words, the lower the singular value, the more likely it is that a set of errors will activate a given MSV, and the larger the activation. This also means that MSVs with lower singular values could see smaller activation in a single inversion, compared to MSVs with higher singular values. It is just statistically less likely to occur.

To dive a little deeper, random errors in the data will have components aligned with the data-space vectors. This includes being aligned with the vectors in the NS. Errors in the latter case would not affect the result, whereas errors aligned with DSVs in the IS are incorporated in the result with a corresponding decrease in data misfit. Using e.g. truncated SVD to reduce the number of MSVs is therefore a suitable way of reducing the influence of such errors, at the cost of not being able to incorporate those MSVs in the result.

4.2 The Influence of Outliers

The influence of outliers is commonly explained using a linear regression example. This example compares the fitting of a line to a number of points, with and without an outlier. When using least-squares regression, the outlier dominates this problem and the resulting line visibly shifts. Although this is an important example to illustrate the importance of managing outliers in gen-

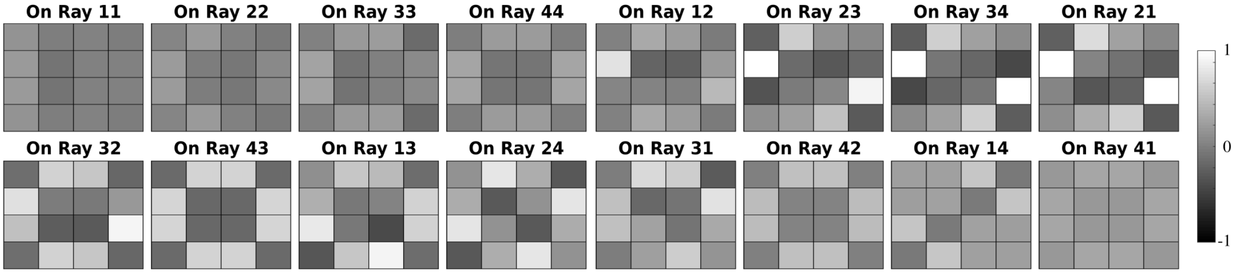

Figure 13. Model results due to outliers. Each subplot shows the final model obtained when only applying a 1 s traveltime (no true data) on a single ray (e.g. R12, which connects shot 1 to receiver 2). The white cells in cases Ray 23, Ray 34, and Ray 21 shoot beyond the colorbar (max. 1.4).

eral, this example is not representative of tomographic problems. Geophysical inversion as described here is rarely over-determined. (Changing the problem's discretization like in e.g. Multi-Dimensional Monte Carlo is one way of making a tomography problem over-determined; Sambridge & Mosegaard, 2002.) To better understand how outliers influence inversion results within the context of this paper, we have set up the following investigation: We apply a 1 s traveltime (a single outlier) to one of the 16 rays in the vertical geometry and invert. Thus this investigation only looks at the direct influence of these outliers without further complicating the problem. Note that the outlier of 1 s is at the same level as the standard deviation of the Gaussian errors in the previous investigation. This is done to get normalized results and thus a comparison between the two investigations needs to be scaled according to a suitable size for an outlier. For investigation j, with the outlier on ray j, we get:

$$Gm = d_j^{outlier}\ , \qquad \text{with } d_j^{outlier} = \begin{cases} 1 \text{ for } i = j \\ 0 \text{ for } i \neq j \end{cases} \tag{9}$$

Fig. 13 shows the 16 estimated models that this investigation produces. As none of the DSVs produce a single traveltime, each outlier is reproduced by a linear combination of several DSVs (thus activating the corresponding MSVs). The linear combination of the activated MSVs show both destructive interference (e.g. rays 11 and 22), and undesired spikes (e.g. rays 23, 34, and 21). Also, MSVs 9 and 12 can clearly be recognized (e.g. in the results for rays 23, 34, and 21, MSV 12 stands out, and an outlier on rays 32 and 43 clearly activates MSV 9).

Fig. 14 shows a summary of the corresponding model weights. Shown are the absolute sums of the weights for each MSV. (The individual results of this investigation are presented in Appendix

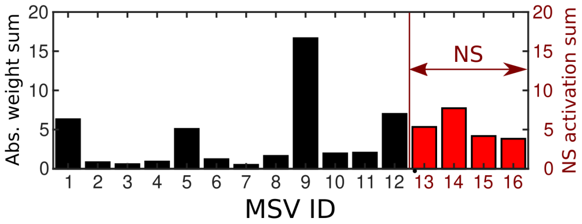

Figure 14. Summary of the outlier inversions. Each inversion has a 1 s outlier on one ray (no true data), which produces weights for each of the Model-Space vectors (MSVs). Shown are the sums of absolute model weights for each MSV ID. The red entries lie in the NS, and instead correspond to the sum of the corresponding Data-Space vector activations.

B.) The outliers preferentially activate MSVs 9, 12, 1, and 5, and there is quite some NS activation. In the latter case, (part of) the outlier does not influence the estimated model. These results show, that there is no relationship between the influence of the outliers and the singular value. For example, the singular values of MSVs 9 and 10 are nearly the same (c.f. Fig. 3), but MSV 9 is obviously much easier activated by an outlier. This further emphasises the importance of good handling of these types of errors, as their effects on the final model is difficult to predict without specifically testing for them.

4.3 How Data Errors Influence Joint, Constrained, and Time-Dependent Inversion

Section 3.2 showed how the activation of certain MSVs is hindered when they contradict the data (IS Contradiction) and unopposed when they do not (NS Transfer). The exact same thing happens with MSVs activated by errors. In the best-case scenario, model errors in one geometry thus contradict the other geometry's data and are opposed, with a resulting increase in data misfit. In the worst-case scenario, model errors are shared between geometries without resistance. Table 3 describes the influence of errors under different circumstances, including when true data is mixed with data errors. For the cases where a single model is produced through Joint inversion, the following needs to be taken into account on top of the entries in Table 3. Data errors that produce IS Contradictions between each other, between themselves and the true data, or both can cause additional NS entries to form (as seen in Case 7 in Fig. 11), as well as cause adjustments that far exceed the influence of the errors on the single inversions (as seen in Case 8 in Fig. 11).

Table 3. Possible influences of errors in combined inversion. **EC(s)**: Error Component(s) **IS**: Image Space, **NS**: Null Space, **DSV(s)**: Data-Space Vector(s), **MSV(s)**: Model-Space Vector(s)

Given	When	Then
Common behaviors	1) ECs fall in the NS of the data	No influence on the models
	2) ECs produce IS Contradictions in the other geometry	MSVs adopted by own geometry and resisted by the other
	3) ECs corroborate the common MSVs	MSVs are adopted by both geometries without resistance
	4) ECs activate MSVs that lie in the NS of the other geometry	MSVs are adopted by both geometries without resistance
Gaussian errors in both datasets		Scenarios 1-4 apply (simultaneously)
One outlier for one geometry		Scenario 3 impossible Scenarios 1, 2, and 4 apply
One outlier each for both geometries		Scenarios 1-4 apply (simultaneously)
Errors and true data	ECs follow the 4 scenarios above	Similar behavior as above superimposed on the behaviors in Figs. 10 and 11
	ECs remove a true data component	True MSV removed from the result
	ECs combine with a true data component to activate a different DSV	True MSV replaced by a different one

5 DISCUSSION

Using visual descriptions and simple representative problems, we have incrementally built up a set of fundamental behaviors of Joint, Constrained, and Time-Dependent inversion, with the goal of providing an intuitive understanding of these abstract and complex methods. The core of these fundamental behaviors can be reduced to two laws: 1) **Inherited model components that do not affect the data misfit will be adopted without resistance.** 2) **Inherited model components that affect the data misfit will be resisted.**

Behaviors like IS Corroboration and NS Transfer arise from the first law, whereas IS Contradictions and component cleaning in non-linear problems arise from the second law. As we have shown, these behaviors also apply to data errors, and the worst cases have data errors contaminate one or both models without resistance. The first law also allows the usage of NS shuttles (e.g., Deal & Nolet 1996). Those, as we have discussed, are used to adjust existing models, whereas the fundamental behaviors we have discussed are fundamentally part of the inversion process. Surprisingly, Joint inversion sometimes produces NS components as a side product of the second law. We suggest that this latter case cannot happen in non-linear inversion, as long as no additional constraints to e.g. an a-priori model are applied. Without any type of constraint, the inversion would have no "power" to resist a change by an intermediate update to a model-component in the current result. For Time-Dependent inversion, we have additionally discussed how changes in the geometry can lead to artificial changes in the results, even when the true model is the same. This is done by having different MSVs in the IS and NS.

Translating these contributions to case-study-level problems will need further investigation. Especially considering the massive 3D problems involving multiple geophysical properties, and differences in parameterization, and differences in spatial/temporal resolution, and differences in error levels and type, and the variety of workflow choices in pre-processing, initial models, and during the non-linear iterations. Fully investigating model-vectors also becomes cost-prohibitive very quickly as the size of the problem increases. Additionally, there are other avenues left unexplored within this range of simple representative problems. Nevertheless, having identified these fundamental behaviors, we can now start applying them.

The rest of this discussion will therefore focus on the following: First, we make hypotheses of how the presented behaviors would interact when using the presented methods simultaneously (e.g. combined non-linear inversion with data errors). Based on that discussion, we will revisit the benefits of producing multiple models simultaneously, over producing a single model with Joint inversion. Then we will dive a little deeper into the relevance to other geophysical methods. Lastly, we will show how inversion results can be improved knowing these fundamental behaviors.

5.1 Predicting Behaviors of Combinations of the Presented Methods

It is beyond the scope of this paper to fully investigate the interactions between the presented phenomena. Though we may not be able to provide a complete picture without such an investigation, the fundamental nature of the presented behaviors does allow us to make some predictions about these interactions below. The ability to setup such hypotheses based on these fundamental behaviors is one of the main contributions of this work. The most important point for the following cases is that changing the problem (by regularization, changing the geometry, or otherwise) will change what data components map onto the IS and NS.

5.1.1 The Influence of Data Errors in Smoothed Inversion

This form of regularization extends the data space (Fig. 7) leading to increased opportunities for data errors to map onto the NS. Therefore, even though the regularized problem can add MSVs that are not contained in the true model (Fig. 6), it should make the inversion more robust against certain data errors.

5.1.2 Combined Inversion Using Smoothing Constraints without Data Errors

Smoothing regularization forces additional model components into each geometry's result (through vector re-orientation). Which components are added will differ between the two geometries. Some of these added components will thus transfer through the NS. These additional differences will also lead to increased opportunity for IS Contradictions. The model components that cause the added IS contradictions are coupled to the true model components. Resisting the contradictions will thus mean resisting the true model components. The strength of this resistance will depend on the size of the data contradictions, and on the level of smoothing. The exception here would be Joint inversion. The smoothing regularization would be added below the two G-kernels in Eq. 6. Thus, the components introduced by smoothing would not lead to an introduction of a corresponding component in the other geometry.

5.1.3 Combined Inversion Using Smoothing Constraints with Data Errors Included

Here, again, the smoothing constraints increase the likelihood of data errors mapping onto the NS (also in Joint inversion). For multi-model producing methods, the increased possibility for IS Contradictions (due to vector re-orientation) should also increase the likelihood that the inversion resists the inclusion of model components due to data errors.

5.1.4 The Influence of Data Errors in Non-Linear Inversion

As non-linear inversion changes what data components map onto the IS and NS when changing the geometry, we would expect that data errors may swap between mapping onto the NS and onto the IS. Thus, data errors could activate MSVs in the intermediate results that transfer through the

NS into the final models. Stated differently, data errors that have already activated components in the intermediate model may no longer show up in the residual for the inversion to act upon. The main issue here, is that data errors could thus influence the path that the inversion takes to the final result. On the other hand, data errors that map onto the NS for a given geometry, are likely still in the residual for the next geometry. This will always depend on the specific case, as data errors that map onto the NS in one intermediate geometry, may already be satisfied by the existing model in the next geometry. If data errors remain in the residual, those that map onto a geometry's IS could remove (part of) MSVs produced in the previous result(s) that might otherwise have been transferred through the NS. Data errors could thus also have a cleaning function. The likelihood of this occurring depends on the size of the data errors, compared to the data components produced by such a MSV and thus relates directly to that MSVs singular value (smaller singular value = more likely).

5.1.5 Smoothed Non-Linear Inversion Without Data Errors

As the geometry changes, the MSVs required to fulfil the smoothing constraints will also change. Thus, these constraints could produce additional components that lie in the NS of the subsequent geometries. At the same time, the newly required components could contradict with components in the previous model and thus (partially) remove them. Thus, smoothing could influence the path towards the final solution in both positive and negative ways.

5.1.6 Smoothed Non-Linear Inversion With Data Errors

Smoothing increases the likelihood that certain data-error components are sent to the NS. As these components likely remain in the residual for the next iteration, these components would repeatedly have the opportunity to affect the IS of the result, except if they are always sent to the NS. Thus, smoothing could lessen the influence of errors, at the cost of the added model components required to fulfil the constraints. At the same time, the effects of the data errors and smoother could combine and push the inversion path into an undesired direction.

5.1.7 Combined Non-Linear Inversion without Data Errors

In combined non-linear inversion, NS components can now also come through the coupling, and in the case of Joint inversion, be produced due to IS Contradictions. Similar to non-linear inversion of a single problem, Joint inversion can (partially) remove such components when contradictions are encountered in either dataset. In contrast, in problems with combined inversion methods that produce multiple models, each sub-problem can only clean their own components. Most problematically, the coupling could allow a component to be reintroduced into a model after a previous cleanup. To explain, we will discuss the case of two non-linear problems, A and B, that are coupled using a combined method that produces a model for each sub-problem. These two sub-problems can swap NS components as follows: 1) a component in result A transfers to result B during one iteration, 2) in a subsequent iteration, problem A cleans out this component as it contradicts the data, whereas it happens to remain in the NS of result B, 3) in a later iteration, problem A once again orients this component in the NS, thus 4) allowing this component to be reintroduced into problem A from problem B.

5.1.8 Combined Non-Linear Inversion with Data Errors Included

Here again, the inclusion of errors increases the possibility of IS Contradictions. Resisting the corresponding model components pushes the associate data-error components into the NS. There, they would be available for the next iteration to produce IS Contradictions again. Also for this case, data-errors could influence the path of the non-linear inversions. This is especially likely when data-errors produce IS Corroboration.

5.1.9 The Last Two Combinations and Other Cases

We invite the reader to hypothesize on how the last two combinations would behave. These are: 1) Combined Non-Linear Inversion Using Smoothing Constraints without Data Errors, and 2) Combined Non-Linear Inversion Using Smoothing Constraints with Data Errors Included. We also invite readers to hypothesize on the following cases, that go beyond the presented investigations: 3) Combined inversions joining three datasets into a single estimated model (e.g. electromagnetics).

4) Combined inversions that produce three or more estimated models (e.g. Vp, Vs, and density in full-waveform inversion, or epochs in time-dependent inversion). 5) Pairwise inter-model constraints in time-dependent inversion, i.e., m1 with m2, m2 with m3, etc.

5.2 Benefits of Producing Multiple Models Simultaneously

The above interactions once again point out the benefit of producing multiple models with a form of constraint between them. This firstly allows us to differentiate between NS Transfer and IS Contradictions through the simple act of comparing models at different levels of regularization. NS Transfer appears at very low level of regularization, whereas IS Contradictions increases with increasing levels of regularization. Then, it helps decrease the influence of data errors on the final results. Lastly, it allows us to check the robustness of features using data subsets, which is always the case for Time-Dependent inversion (see e.g., Hobé et al. 2021).

5.3 Relevance to Other Geophysical Methods

Irrespective of parameterization type (e.g, cell, nodal), if there are the same amount of parameters for the model, then every possible model can be deconstructed with the same MSVs. These MSVs would be distributed differently when the physics changes, similar to how a change in geometry redistributes the MSVs among the IS and NS. Thus, the insights from this paper can be applied directly to investigations where the same method is used with different datasets.

A non-seismic example where the insights of this paper apply is Joint, or Constrained inversion of two different arrays in ERT (e.g. Horo et al. 2021). The physics of ERT would lead to a different redistribution of MSVs among the IS and NS, compared to the seismic example. Similarly to the presented investigations, the problem corresponding to the first ERT array would have MSVs in the NS, that lie in the IS of the second problem, and vise versa.

A translation of these fundamental behaviors is required, however, when coupling geophysical methods using an empirical relationship (e.g. gravimetry and seismics; Haber & Holtzman-Gazit 2013 and references therein) and/or constraints between models with different parameterizations. Filtering behaviors like IS Contradications, NS Transfer, and IS Corroboration through an empirical relationship will make it much more difficult to identify which part of one sub-problem's model influences which part of the other model. However, producing multiple models using different levels of regularization, should also allow us to differentiate between these behaviors. Additional issues may arise when the two sub-problems have different parameterizations. Without further investigation, it is not clear to us how coupling two problems with a different amount of MSVs would affect results. Does a MSV of the sub-problem with less parameters affect multiple MSVs in the other sub-problem? If yes, what happens when both IS and NS components are activated at the same time? If not, are there components in the sub-problem with more parameters that are never affected by the other sub-problem, and do those, vise versa never affect the first sub-problem? Additional difficulties would arise trying to predict these behaviors for methods that change their parameterization during the non-linear inversion process.

5.4 Improving Inversion Results

In this Section, we will describe multiple possibilities for alleviating the severity of Null-Space Contamination and the influence of errors described above. We subdivide these options in the following categories, which we will discuss below: 1) Optimized Experimental Design. 2) Using more and repeater data. 3) Preventing Null-Space Contamination. The most obvious fourth category is the identification, reduction and removal of errors. For this final category, we refer the reader to the literature associated with the individual geophysical methods. One example that reduces picking errors before picking even begins is the "shift and stack" method in active seismics (Park et al. 1996).

5.4.1 Optimized Experimental Design

Lévěque et al. (1993) used the Leveque geometry to great effect to explain the specifics of checkerboard tests. This geometry has also been very helpful in this work to visualize the fundamental behaviors we are interested in. However, this geometry is not the optimal geometry for the 4x4 cell models in question. Here, we will show how all the results in this paper could be improved

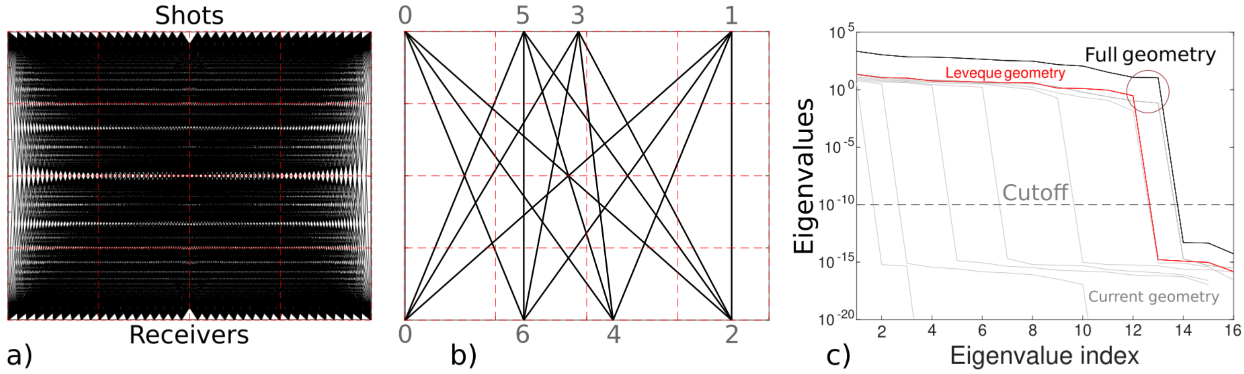

Figure 15. Optimized-Experimental-Design results. **a)** Geometry of all sampled rays. **b)** Optimal geometry obtained for this setup with rays numbered in order of addition (the two zero positions were defined in advance). Red lines in a) and b) denote cell boundaries. **c)** Eigenvalue spectra comparison. The eigenvalues (γ) relate to the singular values (λ) as: $\gamma_i = \lambda_i^2$. The spectra of each OED iteration are shown in grey. The spectrum of the Leveque geometry is shown in red, whereas the spectrum using all rays in a) is shown in black. Eigenvalues below the cutoff are seen as being in the Null Space. The dark-red circle emphasizes the differences of the three spectra for the lowest eigenvalue in the Image Space.

by optimizing the placement of the stations and receivers using Optimized Experimental Design (OED; e.g., Maurer et al. 2010).

At the start of our OED study, we define all possible instrument placements and produce the corresponding rays (Fig. 15a). After defining a starting point (to reduce the computational cost) with a first shot and a first receiver (0 and 0 in Fig. 15b), we search through the remaining shot locations, to find the shot which will maximize the normalized eigenvalue spectrum (Fig. 15c) of the current step (though other criteria exist; Curtis 1999a,b; Routh et al. 2005; Ajo-Franklin 2009; Maurer et al. 2010). This process is repeated, while alternating between shots and receivers, till the desired number of shots and receivers are obtained.

When comparing the three eigenvalue spectra (Fig. 15c) of the Leveque geometry, of the full geometry (using all rays), and the ”optimal” geometry obtained in this way (Fig. 15b), we observe the following: 1) The optimal geometry using 4 shots and 4 receivers elevates one additional singular value above the cutoff compared to the Leveque geometry. 2) The optimal geometry has the same number of MSVs in the IS as the full geometry. 3) The addition of additional rays beyond the optimal geometry further increases the absolute eigenvalues. 4) The number of MSVs in the Image Space obtained using the Leveque geometry can also be obtained using less receivers. Note that the normalized eigenvalue spectrum of the optimal geometry and the full geometry are almost equal (not shown).

To connect back to the influence of errors, OED directly reduces the influence of errors by improving the eigenvalue spectrum. This effect is best seen in Fig. 12, where increasing the singular value leads to a narrowing of these bell curves. Additionally, the elevation of additional MSVs into the IS reduces the opportunity for NS Contamination, and increases the possibility of IS Contradictions. Lastly, the elevation of the entire eigenvalue spectrum for the full geometry shows that the optimal geometry is only optimal from the point of view of the normalized eigenvalue spectrum. The higher spectrum of the full geometry, compared to the optimal geometry, corresponds to a smaller standard deviation of model weights due to Gaussian errors. Similar improvements are expected for the other optimization measures in OED, with these improvements being more localized for measures meant to improve specific model features (e.g. Routh et al. 2005; Ajo-Franklin 2009). Because adding instruments is often more expensive, compared to adding more shots, we will now look at the benefit of adding shots on the same locations for the same instruments.

5.4.2 The Benefit of Additional Data

To show the benefit of additional data, we extend the investigations into the influence of errors as follows. We repeat the rays of the Leveque geometry for each data extension. Then, we either apply Gaussian noise to each ray, or a single outlier on one of the first 16 rays. This is formalized in Eqs 10 and 11 (for investigation j):

$$\begin{bmatrix} G \\ G \\ \vdots \\ G \end{bmatrix} m = \vec{\sigma_e} \tag{10}$$

$$\begin{bmatrix} G \\ G \\ \vdots \\ G \end{bmatrix} m = d_j^{outlier}, \text{ with } d_j^{outlier} = \begin{cases} 1 \text{ for } i = j \\ 0 \text{ for } i \neq j \end{cases}, \text{ for } j < 17 \tag{11}$$

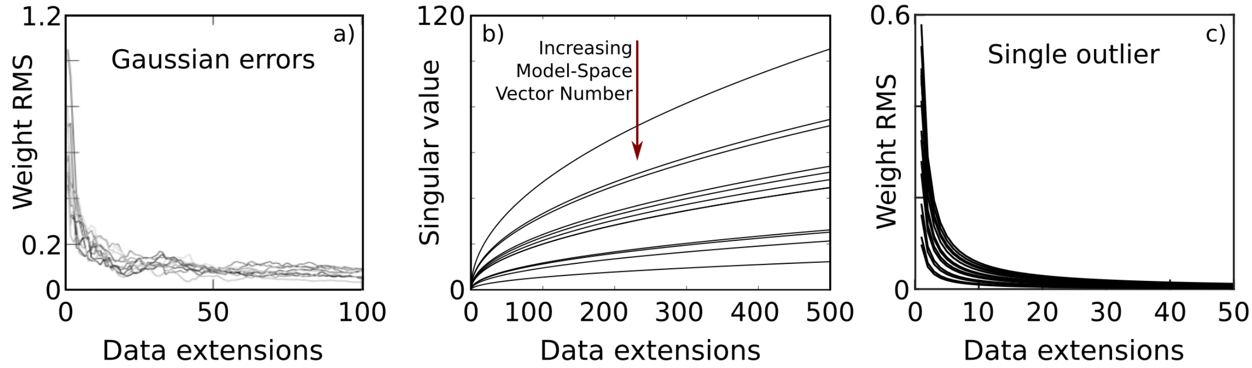

Figure 16. Results for the error investigations when extending data. Each data extension adds the same 16 rays. In **a)** random Gaussian errors are applied to the available rays as traveltimes (errors not repeated). The different curves correspond to ten different seeds. **b)** Shows the Singular values as data increases. In **c)** each curve corresponds to a single outlier being applied to one of the first 16 rays. All other rays for each curve have a 0 s traveltime.

Fig. 16 shows the results. Surprisingly, the influence of errors behaves like an L-curve when using such data extensions. For the first few extensions, the impact on the estimated model rapidly decreases for both investigations. Although the model misfit continues to decrease as more data is added, the rate of decrease declines rapidly. For the outlier investigation, this influence can be summarized to the following equation:

$$R(n) = R_{init}/n \tag{12}$$

Here, R, is the RMS of all the model weights, R_{init}, is the initial value of R, corresponding to the Leveque geometry, and n, is the number of data extensions (n = 1 corresponds to the Leveque geometry).

Fig. 16b shows how the individual singular values improve as we repeat data on the same rays. This result corresponds to both the Gaussian error and outlier investigations. Here, the ability to increase the singular value by adding data on the same rays is clearly correlated with the initial value. A line fit provides the following relationship (Eq 13):

$$\lambda(n) = \lambda_{init} * \sqrt{n} \tag{13}$$

Although the largest initial singular value grows much larger compared to the others, this value was already quite robust against errors to begin with (Fig. 12). The smallest initial singular value (lowest curve) increases rapidly at the beginning, after which the rate of increase declines. As the lower-most curves are the most sensitive to errors, their trend may be enough to explain the L-curve behavior in Fig. 16a and c: While these lower-most curves grow rapidly, the influence of the errors on the most sensitive singular values rapidly decreases. As the growth of these curves decreases, the reduction in error sensitivity decreases as well. Additionally, Eq. 13 means that the conditioning number (largest Singular value divided by the smallest Singular value above the cut-off) remains equal when using extensions with the same rays. Whether this is applicable for extensions using specific subsets of rays will require further investigation.

We show a different aspect of the reduction in error sensitivity in Fig. 17. It shows the DSVs of the case where the rays are sampled twice. While there are 16 MSVs, with four in the NS, there are 32 orthogonal DSVs (one for each traveltime). Each of these vectors has 16 new entries, which are a duplicate of the first 16 for the DSVs in the IS (u1-u12). Most of u17-u32 instead have a single large spike on the right of the red line, along with smaller entries. The relative magnitude of this single spike compared to the other entries increases as we include more data. As there are no singular values associated with these latter 16 DSVs, all of these vectors map onto the NS, and thus do not affect the model. Additional data thus reduces the sensitivity to errors, because there is a greater likelihood for them to map onto the NS (a linear combination of the DSVs can reproduce any data vector). As outliers are unlikely to show up for every repeat observation, it is highly likely that they will map onto one of the large spikes of the DSVs that map onto the NS. Whether there is a maximum amount of outliers per data amount, or whether systematic outliers are more likely to map onto the IS will require further investigation.

As we have shown here, additional data massively reduces the influence of both random Gaussian errors and of single outliers. This reduction occurs through the combined effect of increasing the singular values, and by capturing discrepancies to the IS vectors in an extended NS. The same general behavior is expected from additional data, which does not repeat a previously sampled geometry (e.g. the other rays in Fig. 15a). As Figs. 16a and c look like an L-curve (e.g., Menke 2018), we suggest that such trade-off curves can be used to identify both the minimum and optimum amount of data to collect, as part of an experimental design study. Special versions of OED exist that allow users to optimize for multiple things for a given budget (e.g., Maurer et al. 2010).

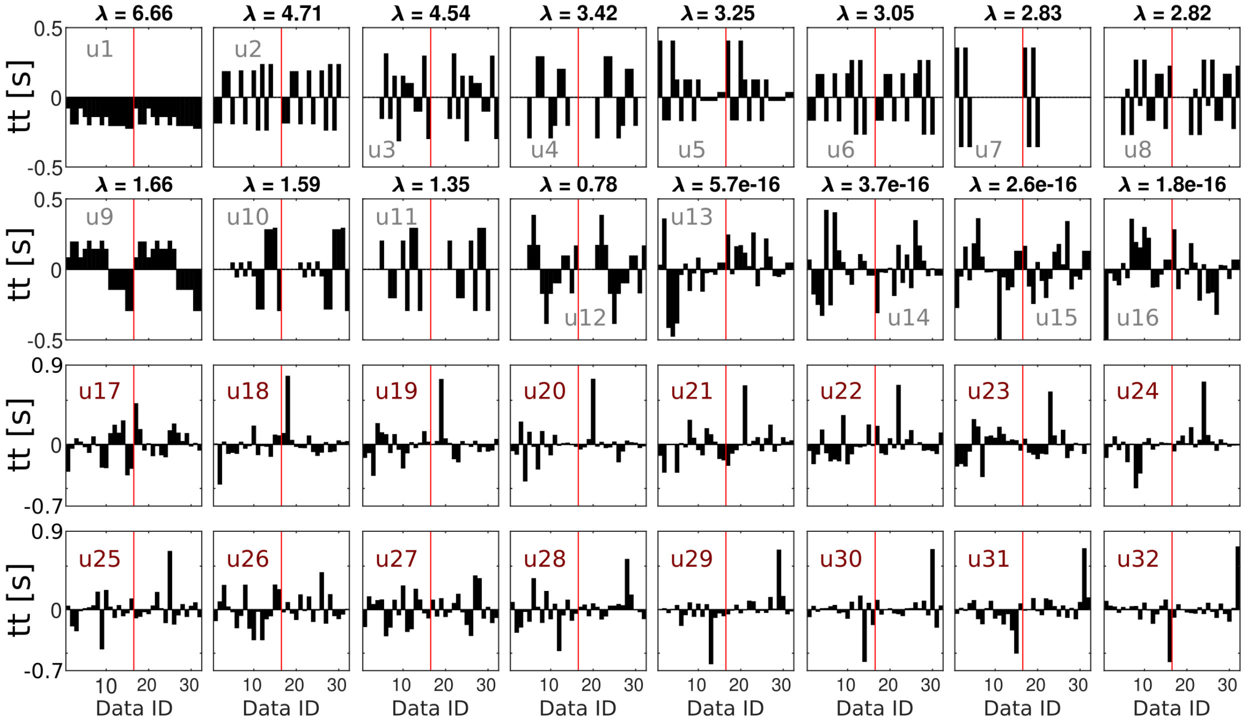

Figure 17. Data-Space vectors for the case where the geometry is duplicated. The red line indicates the start of the duplicated values. Vectors 13-32 map onto the Null Space as there is no singular value (λ) connecting them to a model-space vector.

Thus one could create a method that finds the optimum amount of data for the optimum amount of instruments given the budget and prior knowledge of the area under investigation. To our knowledge, producing an L-curve to identify the optimum amount of data for a given geometry has not previously been discussed.

5.4.3 Preventing Null-Space Contamination

NS Transfer is beneficial when it fills out missing pieces of the true model (given equal true models). However, it also allows the very worst cases of the combined inversion methods (e.g. Case 4 in Figs. 10, and table 2). These cases of NS Contamination become possible, because combined inversion couples these unwanted NS components in one geometry, with IS components in the other geometry. Thus, when the IS components are activated by data in one geometry, the coupling introduces these NS components into the other geometry. NS Contamination can therefore be prevented completely, by removing the coupling of NS components before calculating the estimated models. We discuss three such decoupling strategies in Appendix C, along with a deeper look into how this coupling takes place. We will summarize these strategies here, and show some initial results (Fig. 18). All three strategies start with a comparison of the MSVs in the combined inversion with those in the single inversions for both geometries. The first method uses this comparison to do something similar to truncated SVD, as we truncate coupled MSVs who's entries lie in the NS for both geometries. An additional cleaning step is used when one geometry has more entries in the IS, compared to the other geometry (see Appendix C). In the second method, we use the comparison to purge the NS components of the single inversions from the coupled MSVs. The third method produces the same result in the opposite way. Here, we extract the components that lie in the IS of the single inversions from the coupled MSVs. Fig. 18 compares results of these three strategies against the results of methods where the coupling is intact. Fig. 18 does not show the truncation strategy for Joint inversion. The additional complications arising for this method make this strategy less suitable compared to the purging and IS retention strategies. These latter strategies also need different implementations for Joint inversion because of these complications (see Appendix C).

All three strategies do well preventing NS Transfer for $\alpha = 0.1$. (All results of the NS purging strategy are equivalent to those IS retention method.) Although the truncation strategy is the most practical, Fig. 18 shows that it does not clean out NS Contamination entirely for large α values. The poorer results of the truncation strategy are especially clear for Cases 2-4 ($\alpha = 1$). Case 8 shows the benefit of proper decoupling when trying to differentiate between NS Transfer and IS Contradictions. The coupled results using $\alpha = 1$ include the NS components, whereas the purged results using $\alpha = 1$ only include components in the IS of both geometries. Case 4 shows the added complexity when decoupling of Joint inversion. As Joint inversion only produces one model, we need to choose which NS components to decouple. This can be only those of one geometry (two choices), and the NS components of both geometries at the same time. These choices would also be possible for methods that produce multiple models. In Joint inversion, however, the consequences are more severe. In Fig. 18 we present the Joint inversion strategy, that purges the NS components of both geometries. In Case 4, this results in both true models not mapping onto the final result. For Case 3, only the component in the IS of both geometries is retained. Case 8 shows, that also

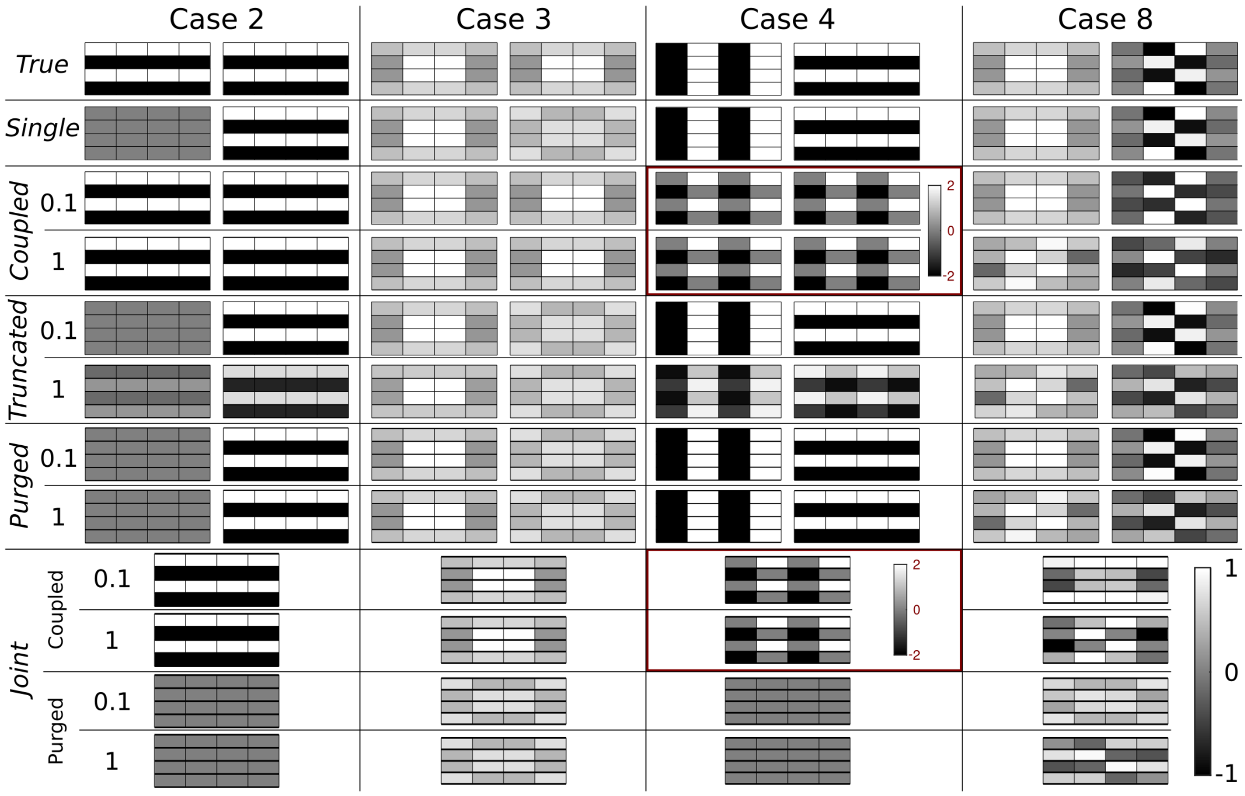

Figure 18. Inversion results comparing decoupling strategies with commonly used combined inversion methods. The top two rows show the True models (one each for the vertical and horizontal geometries), and the results for single inversions of these true models. Then, *Coupled*, *Truncated*, and *Purged* correspond to those strategies applied to inter-model minimization (e.g. epoch damping). The adjacent numbers are the applied regularization factors (α = 0.1 and α = 1). The bottom two rows show the Joint inversion cases. The strategy that retains the IS components produces equivalent results to the purging strategy. Note that the colorbars for the results in the red rectangles differ from all other results. to emphasize the worst case scenario.

the NS components produced due to IS Contradictions are not retained in the final result (also see Case 7 in Fig. 11).

There is one major downside to this decoupling strategy. As it negates NS Transfer between geometries in combined inversion, decoupling not only stops NS Contamination (Case 4 and 8 in Fig. 18); It also stops the transfer of missing components that are common between the true models (Case 2 and 3 in Fig. 18). Nevertheless, the ability to produce separate results with and without NS transfer is very promising. Although it is beyond the scope of this paper, these strategies will need more investigation, even beyond what is shown in C. We suggest that the IS retention strategy has the largest potential. The biggest benefit of decoupling lies in its ability to prevent data-errors in one dataset to transfer through the NS to another sub-problem without resistance. Additional benefits arise in Time-Dependent inversion, where decoupling allows us to focus on differences supported by the data. Lastly, the results in Fig. 18 further emphasize the benefits of producing multiple models using some form of regularization between them, over a single model using Joint inversion.

6 CONCLUSIONS

Using a visual analysis of simple inverse problems, we have shown fundamental behaviors of common inverse methods. Although these problems use traveltimes, the results are applicable to all geophysical methods that use inversion. Before tackling the complex cases, we have, e.g., described the fundamental workings behind the commonly used L-curve, and uncovered the undesired creation of Null-Space (NS) components within non-linear inversion. For Joint, Constrained, and Time-Dependent inversion, we have shown the following three fundamental behaviors: Image-Space (IS) Corroboration, IS Contradictions, and NS Transfer. These fundamental behaviors lead to the following best and worst case scenarios under specific conditions. Best Cases: 1) The reconstruction of equal true models is improved, 2) mixing of unequal true models is resisted, and 3) errors map onto the NS. Worst Cases: 1) Errors map onto the estimated model(s), 2) errors transfer through the NS without resistance, 3) unequal true models mix without affecting the data misfit, and 4) undesired NS components are created when IS contradictions occur in a single model producing Joint inversion.

Based on these insights, we propose multiple avenues to improve inversion results. Next to the common practices for error and outlier removal/reduction, we show that inversion results can be improved using Optimized Experimental Design (OED), incorporating more data, and by decoupling the NS components in the Joint, Constrained, and Time-Dependent inversions. In this context, we present a novel addition to OED, whereby the optimum amount of data can be found after finding the optimum instrument placements, through the use of a trade-off curve showing the influence of errors against the number of data extensions. The decoupling methods are especially useful for Time-Dependent inversions, as it allows us to focus on differences supported by the data, without the influence of NS Transfer.

Overall, we show the benefits of producing multiple estimated models using constraints over combining the inverse problems into a single model. The insights from this paper have the potential to fundamentally improve multiple aspects of geophysical survey design, data pre-processing, model interpretation, and the creation of new inverse methods. More importantly, the visual analysis of simple inverse problems should greatly reduce the difficulty for newcomers and practitioners to improve their intuition of these complex and abstract methods.

7 ACKNOWLEDGEMENTS

We would like to thank Jean-Jacques Lévěque, Luis Rivera, and Gérard Wittlinger for providing the visual clarity in their 1993 publication (e.g., Lévěque et al. 1993). We also thank Jo Boaler for explaining the importance of getting a fundamental sense of a subject, and the importance of presenting it in a variety of ways to activate whole-brain thinking (Boaler 2019). AH's intention to provide his student's with an intuitive sense of geophysical inversion lead to seeing the massive contribution in Lévěque et al. (1993), which further inspired the investigations in this manuscript and those to come. Additional thanks go out to Paula Rulff for providing feedback on an earlier draft of this manuscript. This work was supported by the Swedish strategic research programme StandUp for Energy.

8 DATA AVAILABILITY STATEMENT

No data nor code is made available for this manuscript. We highly recommend reproducing these simple investigations from scratch.

REFERENCES

Ajo-Franklin, J. B., 2009. Optimal experiment design for time-lapse traveltime tomography, *Geophysics*.

Astic, T., Heagy, L. J., & Oldenburg, D. W., 2021. Petrophysically and geologically guided multi-physics inversion using a dynamic gaussian mixture model, *Geophysical Journal International*.

Bloem, E., Forquet, N., Søiland, A., Binley, A., & French, H. K., 2020. Towards understanding time-lapse electrical resistivity signals measured during contaminated snowmelt infiltration, *Near Surface Geophysics*.

Boaler, J., 2019. *Limitless mind: Learn, lead, and live without barriers*, HarperCollins.

Commer, M. & Newman, G. A., 2009. Three-dimensional controlled-source electromagnetic and magnetotelluric joint inversion, *Geophysical Journal International*.

Curtis, A., 1999a. Optimal design of focused experiments and surveys, *Geophysical Journal International*.

Curtis, A., 1999b. Optimal experiment design: cross-borehole tomographic examples, *Geophysical Journal International*.

de la Varga, M., Schaaf, A., & Wellmann, F., 2019. Gempy 1.0: open-source stochastic geological modeling and inversion, *Geoscientific Model Development*.

De Wit, R., Trampert, J., & Van Der Hilst, R., 2012. Toward quantifying uncertainty in travel time tomography using the null-space shuttle, *Journal of Geophysical Research: Solid Earth*.

Deal, M. M. & Nolet, G., 1996. Nullspace shuttles, *Geophysical Journal International*.

Demirci, İ., Dikmen, Ü., & Candansayar, M. E., 2018. Two-dimensional joint inversion of magnetotelluric and local earthquake data: Discussion on the contribution to the solution of deep subsurface structures, *Physics of the Earth and Planetary Interiors*.

Doetsch, J., Linde, N., Coscia, I., Greenhalgh, S. A., & Green, A. G., 2010. Zonation for 3d aquifer characterization based on joint inversions of multimethod crosshole geophysical data, *Geophysics*.

Fichtner, A. & Zunino, A., 2019. Hamiltonian nullspace shuttles, *Geophysical research letters*.

Fichtner, A., Zunino, A., Gebraad, L., & Boehm, C., 2021. Autotuning hamiltonian monte carlo for efficient generalized nullspace exploration, *Geophysical Journal International*.

Gallardo, L. A., 2007. Multiple cross-gradient joint inversion for geospectral imaging, *Geophysical Research Letters*.

Gallardo, L. A. & Meju, M. A., 2004. Joint two-dimensional dc resistivity and seismic travel time inversion with cross-gradients constraints, *Journal of Geophysical Research: Solid Earth*.

Gallardo, L. A. & Meju, M. A., 2007. Joint two-dimensional cross-gradient imaging of magnetotelluric and seismic traveltime data for structural and lithological classification, *Geophysical Journal International*.

Haber, E. & Holtzman-Gazit, M., 2013. Model fusion and joint inversion, *Surveys in Geophysics*.

Hardt, M. & Scherbaum, F., 1994. The design of optimum networks for aftershock recordings, *Geophysical Journal International*.

Hellman, K., Ronczka, M., Günther, T., Wennermark, M., Rücker, C., & Dahlin, T., 2017. Structurally coupled inversion of ert and refraction seismic data combined with cluster-based model integration, *Journal of Applied Geophysics*.

Hobé, A., Gudmundsson, O., Tryggvason, A., & group, S. S., 2021. Imaging the 2010-2011 Inflationary Source at Krysuvik, SW Iceland, Using Time-Dependent Vp/Vs Tomography, in *Proceedings World Geothermal Congress 2020+1*.

Horo, D., Pal, S. K., & Singh, S., 2021. Mapping of gold mineralization in ichadih, north singhbhum mobile belt, india using electrical resistivity tomography and self-potential methods, *Mining, Metallurgy*

& Exploration.

Jousset, P., Haberland, C., Bauer, K., & Arnason, K., 2011. Hengill geothermal volcanic complex (iceland) characterized by integrated geophysical observations, *Geothermics*.

Julia, J., Ammon, C., Herrmann, R., & Correig, A. M., 2000. Joint inversion of receiver function and surface wave dispersion observations, *Geophysical Journal International*.

Julian, B. R. & Foulger, G. R., 2010. Time-Dependent Seismic Tomography, *Geophysical Journal International*.

Koulakov, I., Gordeev, E. I., Dobretsov, N. L., Vernikovsky, V. A., Senyukov, S., Jakovlev, A., & Jaxybulatov, K., 2013. Rapid changes in magma storage beneath the klyuchevskoy group of volcanoes inferred from time-dependent seismic tomography, *Journal of Volcanology and Geothermal Research*.

Kraft, T., Mignan, A., & Giardini, D., 2013. Optimization of a large-scale microseismic monitoring network in northern switzerland, *Geophysical Journal International*.

Lévěque, J.-J., Rivera, L., & Wittlinger, G., 1993. On the Use of the Checker-Board Test to Assess the Resolution of Tomographic Inversions, *Geophysical Journal International*.

Linde, N., Binley, A., Tryggvason, A., Pedersen, L. B., & Revil, A., 2006. Improved hydrogeophysical characterization using joint inversion of cross-hole electrical resistance and ground-penetrating radar traveltime data, *Water Resources Research*.

Malehmir, A., Andersson, M., Mehta, S., Brodic, B., Munier, R., Place, J., Maries, G., Smith, C., Kamm, J., Bastani, M., et al., 2016. Post-glacial reactivation of the Bollnäs fault, central Sweden–a multidisciplinary geophysical investigation, *Solid Earth*.

Manukyan, E., Maurer, H., & Nuber, A., 2018. Improvements to elastic full-waveform inversion using cross-gradient constraints, *Geophysics*.

MATLAB, 2021. *9.11.0.1809720 (R2021b)*, The MathWorks Inc., Natick, Massachusetts.

Maurer, H., Curtis, A., & Boerner, D. E., 2010. Recent Advances in Optimized Geophysical Survey Design, *Geophysics*.

Menke, W., 2018. *Geophysical data analysis: Discrete inverse theory*, Academic press.

Moorkamp, M., Heincke, B., Jegen, M., Roberts, A. W., & Hobbs, R. W., 2011. A framework for 3-d joint inversion of mt, gravity and seismic refraction data, *Geophysical Journal International*.

Park, C. B., Miller, R. D., Steeples, D. W., & Black, R. A., 1996. Swept impact seismic technique (sist), *Geophysics*.

Paulatto, M., Moorkamp, M., Hautmann, S., Hooft, E., Morgan, J. V., & Sparks, R. S. J., 2019. Vertically extensive magma reservoir revealed from joint inversion and quantitative interpretation of seismic and gravity data, *Journal of Geophysical Research: Solid Earth*.

Rawlinson, N. & Spakman, W., 2016. On the use of sensitivity tests in seismic tomography, *Geophysical Journal International*, pp. 1221–1243.

Rawlinson, Z., Townend, J., Arnold, R., & Bannister, S., 2012. Derivation and implementation of a nonlinear experimental design criterion and its application to seismic network expansion at kawerau geothermal field, new zealand, *Geophysical Journal International*.

Routh, P. S., Oldenborger, G. A., & Wang, D. W., 2005. Optimal survey design using the point spread function measure of resolution, in *2005 SEG Annual Meeting*, OnePetro.

Rowbotham, P. S. & Pratt, R. G., 1997. Improved inversion through use of the null space, *Geophysics*.

Rücker, C., Günther, T., & Wagner, F. M., 2017. pygimli: An open-source library for modelling and inversion in geophysics, *Computers & Geosciences*.

Sambridge, M. & Mosegaard, K., 2002. Monte carlo methods in geophysical inverse problems, *Reviews of Geophysics*.

Sharipov, R., 2004. Course of linear algebra and multidimensional geometry, *arXiv preprint math/0405323*.

Soyer, W., Mackie, R., Hallinan, S., Pavesi, A., Nordquist, G., Suminar, A., Intani, R., & Nelson, C., 2018. Geologically consistent multiphysics imaging of the darajat geothermal steam field, *First Break*.

Tryggvason, A. & Linde, N., 2006. Local earthquake (le) tomography with joint inversion for p-and s-wave velocities using structural constraints, *Geophysical Research Letters*.

Tso, C.-H. M., 2019. *Enhancing the information content of geophysical data for nuclear site characterisation*, Lancaster University (United Kingdom).

Vozoff, K. & Jupp, D., 1975. Joint inversion of geophysical data, *Geophysical Journal International*.

Wagner, D., Koulakov, I., Rabbel, W., Luehr, B.-G., Wittwer, A., Kopp, H., Bohm, M., Asch, G., & scientists, M., 2007. Joint inversion of active and passive seismic data in central java, *Geophysical Journal International*.

Wagner, F., Mollaret, C., Günther, T., Kemna, A., & Hauck, C., 2019. Quantitative imaging of water, ice and air in permafrost systems through petrophysical joint inversion of seismic refraction and electrical resistivity data, *Geophysical Journal International*.

Zhou, J., Meng, X., Guo, L., & Zhang, S., 2015. Three-dimensional cross-gradient joint inversion of gravity and normalized magnetic source strength data in the presence of remanent magnetization, *Journal of Applied Geophysics*.

APPENDIX A: IN-DEPTH SMOOTHING CONSTRAINTS INVESTIGATION RESULTS

In Fig. 8 (Section 3.1.4), we only showed the model weights for four reconstructions using smoothed inversion. The results for all 12 data-producing MSV are shown in Figs. A1 and A2.

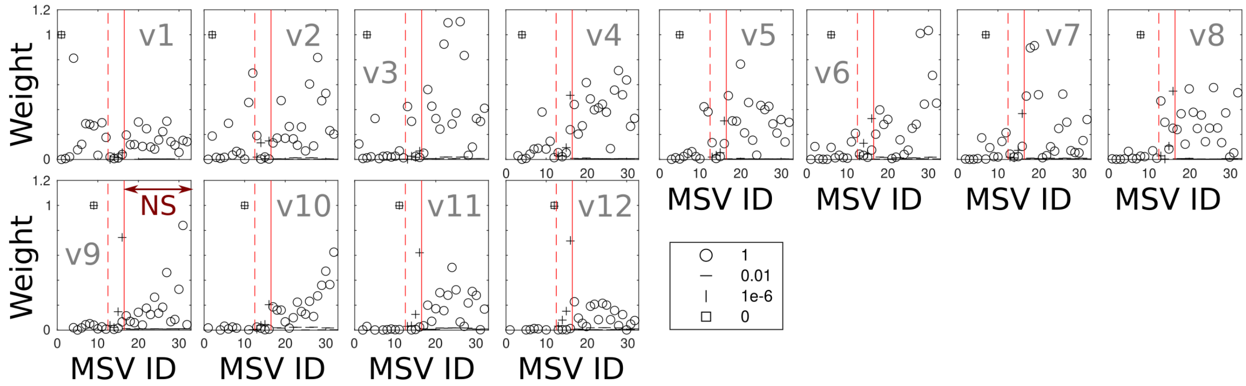

Figure A1. Inversion results for reconstructing true models (V1-V12 here) in Fig. 3 using the vertical geometry and different levels of smoothing. V13-16 are not shown as they do not produce traveltime data. To the left of the full red line, these subplots show the absolute weights for each of the model-space vectors (MSVs) of the smoothed vertical problem, i.e., these values show how much of each MSV (values on the x-axes) is used when inverting for a given true model (e.g. V1) using different levels of smoothing. The MSV IDs to the right of the full red line instead show how much of the data is captured by the Null Space (NS) of the data space, i.e. the absolute data length in the direction of that DSV in the NS. Values between the broken red line and the full red line correspond to the four MSVs that are in the NS for the original problem. These are no longer in the NS for the smoothed problem, as small Image-Space components have been added that now activate these MSVs using data. Here, all values have been truncated below 1e-3.

APPENDIX B: IN-DEPTH OUTLIER INVESTIGATION RESULTS

For story purposes, we did not go into depth in Section 4.2. Here, we present and discuss the individual results of the single outlier investigation using only the vertical geometry. As a reminder, we apply a 1 s traveltime to a single ray (a single outlier) and invert for that data without adding any other data.

Fig. B1 shows the resulting weights on the individual MSVs for each affected ray. Here, the rays are ordered as implemented from left to right, with the two numbers corresponding to the shot and receiver that the ray links together (e.g. R34 has shot 3 and receiver 4). As none of the DSVs

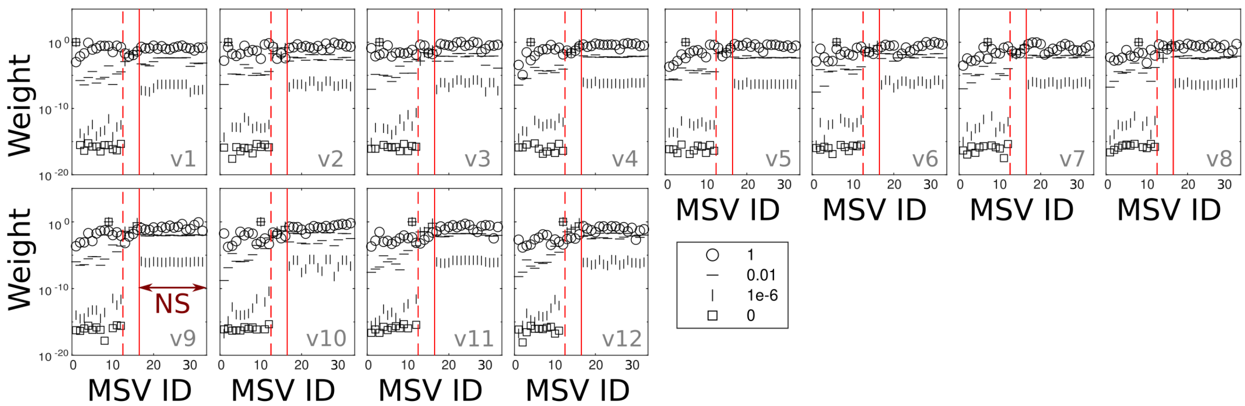

Figure A2. Log-linear view of Fig. 8 without truncation.

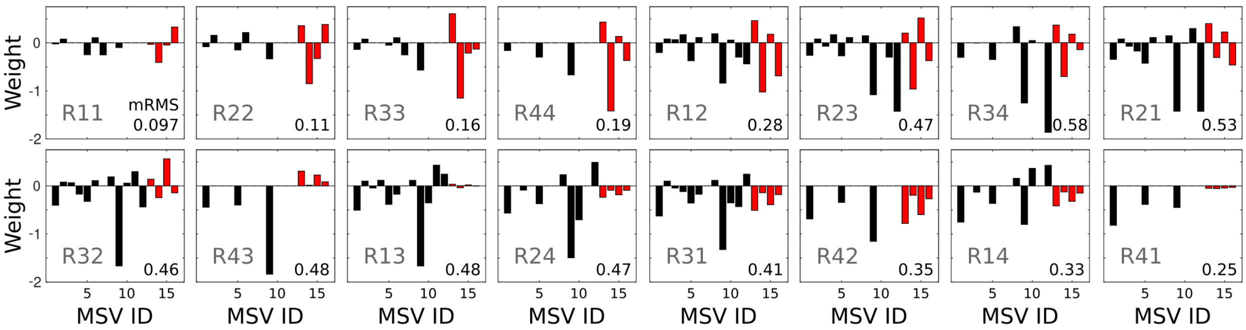

Figure B1. Model weights activated by an outlier on a single ray (e.g. R12, which connects shot 1 to receiver 2). The x-axis shows which model-space vector is activated, whereas the y-axis denotes how much it is activated. The red entries correspond to Null-Space vectors. These red values correspond to how much the corresponding data-space vector is activated. The number in the corner of each subplot shows the resulting model RMS misfit.

produce a single traveltime, each outlier is reproduced by a linear combination of several DSVs (thus activating the corresponding MSVs). Fig. B1 shows that the outliers preferentially activate MSV 9 and MSV 12, similarly to what we saw in the Fig. 14.

The resulting models presented in Fig. 13 are summarized as model RMS misfits in Fig. B1. (As there is no true data, the results should be zeros everywhere.) These mRMS values again show, that individual outliers on the vertical rays (11, 22, 33, and 44) have the smallest impact on the final result. This is followed by the steepest diagonal rays (14 and 41).

Fig. B2 shows that the sensitivity of the individual MSVs to single outliers depends on which ray is affected. Interestingly, the influence of the outlier does not scale with the singular value, as per the common rule for errors (e.g., Menke 2018). MSV 7 is only affected with outliers on rays 1 and 3, whereas e.g. MSV 5 is always affected. Here also, MSVs 9 and 12 show the largest weights.

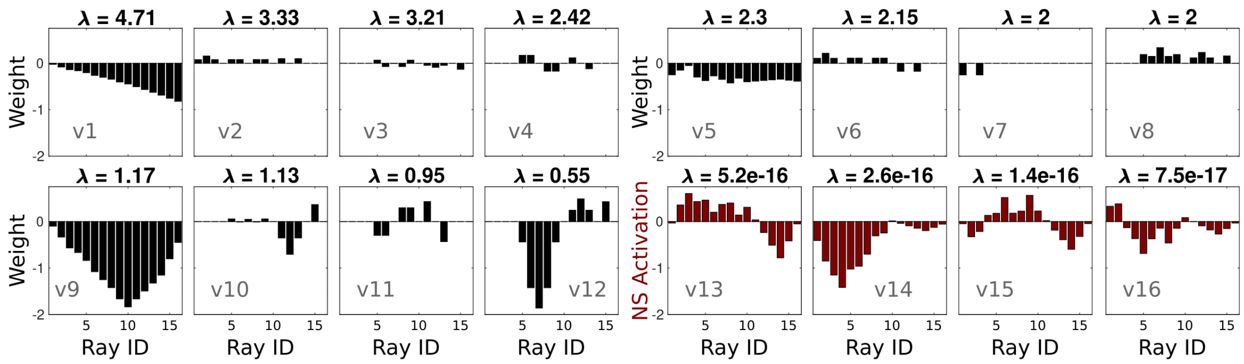

Figure B2. Model-Space vector (MSV) activation by an outlier on a single ray (Ray order according to Fig. B1 from left to right). The x-axis shows which ray has the outlier, whereas the y-axis denotes how much each MSV (e.g. v1) is activated. For the red entries (v13-v16), the length of the outlier in the direction of the data-space vector is depicted instead, as these vectors lie in the Null Space.

We could not think of a clear reason why MSV 9 and MSV 12 should preferentially be activated by such outliers. Nor, do we see a clear behavior here, which we could point out. The main point of presenting these additional Figures, is that outliers do not behave the way they are commonly explained (e.g. deviation in fitting a line, nor inverse proportional to the singular value).

APPENDIX C: DECOUPLING STRATEGIES

NS Transfer can be prevented by decoupling sub-components of MSVs in a geometry's NS. To get a better understanding of what this means, we first need to dive into the decomposition of the combined inversion problems. We will first present the examples for combined inversion methods that produce multiple models, before explaining the alternate case for Joint inversion. For a method that produces multiple models, when we apply SVD to both geometries simultaneously, without applying any regularization (i.e. set $\alpha = 0$ in Eq. 7), this solves the two problems separately as we can see in Eq. C.1 and C.2. Each column of $U_{no\_regularization}$ and $V_{no\_regularization}$ either solves for the first, or for the second geometry (hence the two rows in each equation).

$$V_{no\_regularization} = \begin{pmatrix} \overrightarrow{v_{11a}} & \overrightarrow{0} & \overrightarrow{v_{12a}} & \overrightarrow{0} & \cdots & \overrightarrow{v_{1ia}} & \overrightarrow{0} & |\overrightarrow{v_{1NS}} & \overrightarrow{0} & \cdots \\ \overrightarrow{0} & \overrightarrow{v_{21a}} & \overrightarrow{0} & \overrightarrow{v_{22a}} & \cdots & \overrightarrow{0} & \overrightarrow{v_{2ia}} & \overrightarrow{0} & \overrightarrow{v_{2i+1a}} & |\overrightarrow{v_{2NS}} \end{pmatrix} \tag{C.1}$$

$$U_{no\_regularization} = \begin{pmatrix} \overrightarrow{u_{11a}} & \overrightarrow{0} & \overrightarrow{u_{12a}} & \overrightarrow{0} & \cdots & \overrightarrow{u_{1ia}} & \overrightarrow{0} & |\overrightarrow{u_{1NS}} & \overrightarrow{0} & \cdots \\ \overrightarrow{0} & \overrightarrow{u_{21a}} & \overrightarrow{0} & \overrightarrow{u_{22a}} & \cdots & \overrightarrow{0} & \overrightarrow{u_{2ia}} & \overrightarrow{0} & \overrightarrow{u_{2i+1a}} & |\overrightarrow{u_{2NS}} \end{pmatrix} \tag{C.2}$$

Here, $\overrightarrow{v}$, corresponds to a sub-vector of V, and $\overrightarrow{u}$, corresponds to a sub-vector of U. The first index denotes which geometry this sub-vector maps onto, and the second index denotes the singular value index for the single geometry case. The last entry denotes if this sub-vector is native to the geometry of the first index (a), or if this sub-vector fills in the constraints associated with a native vector in the other geometry (b, see e.g. Eq. C.3). $\overrightarrow{u_{24a}}$ thus denotes the fourth DSV mapped onto the 2nd geometry dominated by that geometry. The vertical bar denotes the cutoff for the NS, and $\overrightarrow{v_{1NS}}$, corresponds to a MSV for geometry 1 in the NS. Note that the IS of two geometries do not need to have the same amount of MSVs, nor DSVs (like is the case for the geometries in Fig. 2).

The solutions for the sub-problems become coupled when we apply a regularization (Eqs. C.3 and C.4):

$$V_{combined} = \begin{pmatrix} \overrightarrow{v_{11a}} & \overrightarrow{v_{11b}} & \overrightarrow{v_{12a}} & \overrightarrow{v_{12b}} & \cdots & \overrightarrow{v_{1ia}} & \overrightarrow{v_{1ib}} & |\overrightarrow{v_{1NS}} & \cdots & \cdots \\ \overrightarrow{v_{21b}} & \overrightarrow{v_{21a}} & \overrightarrow{v_{22b}} & \overrightarrow{v_{22a}} & \cdots & \overrightarrow{v_{2ib}} & \overrightarrow{v_{2ia}} & \overrightarrow{v_{2i+1b}} & \overrightarrow{v_{2i+1a}} & |\overrightarrow{v_{2NS}} \end{pmatrix} \tag{C.3}$$

$$U_{combined} = \begin{pmatrix} \overrightarrow{u_{11a}} & \overrightarrow{u_{11b}} & \overrightarrow{u_{12a}} & \overrightarrow{u_{12b}} & \cdots & \overrightarrow{u_{1ia}} & \overrightarrow{u_{1ib}} & |\overrightarrow{u_{1NS}} & \cdots & \cdots \\ \overrightarrow{u_{21b}} & \overrightarrow{u_{21a}} & \overrightarrow{u_{22b}} & \overrightarrow{u_{22a}} & \cdots & \overrightarrow{u_{2ib}} & \overrightarrow{u_{2ia}} & \overrightarrow{u_{2i+1b}} & \overrightarrow{u_{2i+1a}} & |\overrightarrow{u_{2NS}} \\ \overrightarrow{l_1} & \overrightarrow{l_2} & \overrightarrow{l_3} & \overrightarrow{l_4} & \cdots & \overrightarrow{l_j} & \overrightarrow{l_{j+1}} & \cdots & \cdots & \cdots \end{pmatrix} \tag{C.4}$$

In Eq. C.3, the $\overrightarrow{0}$ below $\overrightarrow{v_{11a}}$ has been replaced with $\overrightarrow{v_{21b}}$. Thus, the corresponding singular value is now shared by two sub-vectors. One that maps onto geometry 1 and one that maps onto geometry 2. This means that, whenever $\overrightarrow{v_{11a}}$ is included in the first model, $\overrightarrow{v_{21b}}$ is included in the second model. Eq. C.4 shows a similar adjustment, where the new sub-vector $\overrightarrow{u_{21b}}$ is the normalized data for the sub-vector $\overrightarrow{v_{21b}}$. $U_{combined}$ also has a third sub-vector, $\overrightarrow{l_i}$, which contains the regularization values, similar to the Laplacian values seen in Fig. 7. Note that the order of the vectors depends on the new singular values. Thus, a vector dominated by geometry 2 could come before one dominated by geometry 1. Each column will always have an ”a” and ”b” pair, however.

In Eqs. C.3, $\overrightarrow{v_{1NS}}$, again corresponds to a MSV for geometry 1 in the NS for single inversion case. We define it in this way, as these vectors take part in the contamination. In the combined inversion, the corresponding singular value is no longer below the cutoff (due to the regularization), and thus no longer identifiable as being in the NS of our observables. This larger singular value allows the NS Transfer to occur.

C1 Decoupling Trough Truncation With Cleanup

Because NS Transfer occurs when a MSV in a geometry's NS is added to that geometry's result, setting just these vectors back to $\overrightarrow{0}$ goes a long way towards negating NS transfer. Eq. C.5 presents this strategy for methods that produce multiple models:

$$V_{decoupled} = \begin{pmatrix} \overrightarrow{v_{11a}} & \overrightarrow{v_{11b}} & \overrightarrow{v_{12a}} & \overrightarrow{v_{12b}} & \cdots & \overrightarrow{v_{1ia}} & \overrightarrow{v_{1ib}} \mid & \cancel{\overrightarrow{v_{1NS}}}\ \overrightarrow{0} & \overrightarrow{0} & \overrightarrow{0} \\ \overrightarrow{v_{21b}} & \overrightarrow{v_{21a}} & \overrightarrow{v_{22b}} & \overrightarrow{v_{22a}} & \cdots & \overrightarrow{v_{2ib}} & \overrightarrow{v_{2ia}} & \overrightarrow{v_{2i+1a}} & \overrightarrow{v_{2i+1b}} \mid & \cancel{\overrightarrow{v_{2NS}}}\ \overrightarrow{0} \end{pmatrix} \tag{C.5}$$

When vectors of both geometries are in their respective NS for the individual inversions, these vectors can also be truncated completely. Because the singular values have been elevated, using them as truncation criteria for this purpose will not ensure all NS components have been decoupled. As changing the problem also reorients the MSVs (as we have seen in Section 3.1.4), the truncation strategy is unable to fully remove the coupling of all NS components. This is especially evident for high α values (Fig. 18).

C2 Decoupling By Purging Null-Space Entries

In this strategy, we completely remove the components that lie in the NS for the single inversions from $V_{combined}$. This is formalized in Eqs. C.6 and C.7:

$$v_{1,i,j}^{decoupled} = v_{1,i,j} - \sum_{k=1}^{m} \frac{v_k^{NS1} \cdot v_{1,i,j}}{v_k^{NS1} \cdot v_k^{NS1}} \cdot v_k^{NS1} \tag{C.6}$$

$$v_{2,i,j}^{decoupled} = v_{2,i,j} - \sum_{k=1}^{n} \frac{v_k^{NS2} \cdot v_{2,i,j}}{v_k^{NS2} \cdot v_k^{NS2}} \cdot v_k^{NS2} \tag{C.7}$$

Here, v_k^{NS1}, are the MSVs in the NS of the single inversion for the first geometry, and, $v_{1,i,j}$ is the sub-vector of $V_{combined}$ (e.g. $\overrightarrow{V11a}$) corresponding to geometry 1. The sums use m and n, respectively, to signify that the geometries could have different numbers of MSVs in the NS.

Because this strategy only changes the V matrix, the model weights of the combined problem are not changed. Instead, the corresponding MSVs are included equal to the coupled problem, minus the NS entries. Thus the estimated models produced will not have the NS Transfer occur, and will otherwise be the same as the original combined problem.

The purging strategy is not very practical, as it requires all NS entries. This is addressed in the third strategy, which produces equivalent results up to machine precision.

C3 Decoupling By Retaining Image-Space Entries

One can get the same $v^{decoupled}$ by summing the components in the IS of the single inversions. This is formalized in Eqs. C.8 and C.9:

$$v_{1,i,j}^{decoupled} = \sum_{k=1}^{m} \frac{v_k^{IS1} \cdot v_{1,i,j}}{v_k^{NS1} \cdot v_k^{NS1}} \cdot v_k^{NS1} \tag{C.8}$$

$$v_{2,i,j}^{decoupled} = \sum_{k=1}^{n} \frac{v_k^{IS2} \cdot v_{2,i,j}}{v_k^{NS2} \cdot v_k^{NS2}} \cdot v_k^{NS2} \tag{C.9}$$

This only requires the MSVs of the single inversions, making this strategy much more tractable.

C4 Decoupling NS Entries in Joint inversion

Joint inversion differs in two ways: The regularization is applied to the equations of one geometry, and only a single model is produced. Thus, no additional entry for the constraints is added to the DSVs (l_i in Eq. C.4), and the model-space vectors are not subdivided into an ”a” and ”b” pair. Therefore, the three strategies need to be implemented differently. For Joint inversion, all strategies need a decision on which NS components are to be decoupled: those of both geometries, or just of one. This choice will likely depend on the range of regularization values relevant to the problem. Both the purging strategy and the IS retention strategy then adjust the V matrix accordingly. (There will be only 1 sub-vector, corresponding to one model, so the chosen components of both geometries are applied to this one sub-vector.) Note, that adjusting the components of only one geometry is also possible for combined inversion methods that produce multiple models. In Joint inversion, this may make more sense to do, whereas more insights are gained for multi-model producing methods by adjusting the components of both geometries.

Eqs C.10 - C.12 formalizes the NS purging strategy for Joint inversion, and Eqs. C.13 - C.15 formalize the IS retention for Joint inversion.

$$v_i^{decoupled,1} = v_i - \sum_{k=1}^{m} \frac{v_k^{NS1} \cdot v_i}{v_k^{NS1} \cdot v_k^{NS1}} \cdot v_k^{NS1} \tag{C.10}$$

$$v_i^{decoupled,2} = v_i - \sum_{k=1}^{n} \frac{v_k^{NS2} \cdot v_i}{v_k^{NS2} \cdot v_k^{NS2}} \cdot v_k^{NS2} \tag{C.11}$$

$$v_i^{decoupled,both} = v_i^{decoupled,1} - \sum_{k=1}^{m} \frac{v_k^{NS2} \cdot v_i^{decoupled,1}}{v_k^{NS2} \cdot v_k^{NS2}} \cdot v_k^{NS2} \tag{C.12}$$

$$v_i^{decoupled,1} = \sum_{k=1}^{m} \frac{v_k^{IS1} \cdot v_i}{v_k^{NS1} \cdot v_k^{NS1}} \cdot v_k^{NS1} \tag{C.13}$$

$$v_i^{decoupled,2} = \sum_{k=1}^{n} \frac{v_k^{IS2} \cdot v_i}{v_k^{NS2} \cdot v_k^{NS2}} \cdot v_k^{NS2} \tag{C.14}$$

$$v_i^{decoupled,both} = \sum_{k=1}^{n} \frac{v_k^{IS2} \cdot v_i^{decoupled,1}}{v_k^{NS2} \cdot v_k^{NS2}} \cdot v_k^{NS2} \tag{C.15}$$

The truncation strategy makes less sense for Joint inversion. This method causes the following two issues to arise when trying to implement this strategy: 1) When α values are low, the singular values are dominated by one geometry. The singular values thus do not provide information on where the components of the other geometry are located. Purging or retaining such components will therefore not be straightforward. It will essentially require the same work as the NS purging and IS retention strategies, with lesser performance (see the *Truncated* epoch-damping results in Fig. 18). 2) The regularization can cause the order of the vectors to change relative to the single inversions. Therefore, starting the truncation at the same vector index may not lead to removing the undesired components, and some desired components may be removed instead. Thus, the truncation method likely produces poorer performance in Joint inversion, compared to the same strategy applied to multi-model producing methods. We even expect poorer performance when only adjusting the dominant geometry's components at low α values.

C5 What About Adjusting S and U?

The NS purging and IS retention strategies change the MSVs in the V matrix, without making any adjustments to the singular values in the S matrix, nor the DSVs in the U matrix. Leaving the S and U matrices untouched equates to forcing a different answer to the same question. We have investigated what happens when recalculating S and U based on the new V matrix: $V_{decoupled}$. Here, we first normalize the MSVs in $V_{decoupled}$, which is not done in the strategies described above. Next, we calculate the synthetic data produced by $V_{decoupled}^{normalized}$, by multiplying it with the appropriate kernel (left-hand-side kernel in either Eq. 6 or 7). When α is non-zero, this will also produce the constraint values when using Eq. 7. This synthetic data is then normalized again, to produce the DSVs for the new U matrix: $U_{decoupled}$. The factors required to normalize the individual DSVs correspond to the inverse of the new singular values, which go into $S_{decoupled}$. Eqs. C.16 - C.18 formalize the creation and normalization of the U, S, and V matrices:

$$v_i^{normalized} = \frac{v_i}{v_i \cdot v_i} \tag{C.16}$$

$$\lambda_i = u_i \cdot u_i \tag{C.17}$$

$$u_i^{normalized} = \frac{u_i}{\lambda_i} \tag{C.18}$$

The new set of matrices asks a different question of the data, and thus produces different results, compared to the NS purging and IS retention strategies. Although the normalized versions of these two strategies successfully prevent NS Transfer, the results sometimes differ strongly from the previous strategies, resulting in a poorer performance. Thus we recommend the previous strategies over setting up a self-consistent question (i.e. matching U, S, and V matrices).

C6 Unknown Consequences

These decoupling strategies need further investigation. It is, for example, not clear to us how NS purging and IS retention needs to be implemented (and what the consequences would be) when smoothing regularization is applied. An optimal integration of these strategies into a non-linear combined inversion will also need to be found.